

Geophysical & Astrophysical Fluid Dynamics



ISSN: 0309-1929 (Print) 1029-0419 (Online) Journal homepage: www.tandfonline.com/journals/ggaf20

Radiatively-cooled moist convection under idealised climate change scenarios: linear analysis

G. N. Dritschel, S. M. Tobias, D. J. Parker & L. Tomassini

To cite this article: G. N. Dritschel, S. M. Tobias, D. J. Parker & L. Tomassini (10 Nov 2025): Radiatively-cooled moist convection under idealised climate change scenarios: linear analysis, Geophysical & Astrophysical Fluid Dynamics, DOI: 10.1080/03091929.2025.2556358

To link to this article: https://doi.org/10.1080/03091929.2025.2556358

9	© 2025 The Author(s). Published by Informa UK Limited, trading as Taylor & Francis Group
	Published online: 10 Nov 2025.
	Submit your article to this journal $oldsymbol{oldsymbol{\mathcal{G}}}$
ılıl	Article views: 55
a ^r	View related articles 🗗
CrossMark	View Crossmark data ☑







Radiatively-cooled moist convection under idealised climate change scenarios: linear analysis

G. N. Dritschel [©] ^a, S. M. Tobias [©] ^a, D. J. Parker ^{a,b,c} and L. Tomassini ^{a,d}

^aSchool of Mathematics, University of Leeds, Leeds, UK; ^bNORCE Norwegian Research Centre AS, Bergen, Norway; CNCAS National Centre for Atmospheric Science, University of Leeds, Leeds, UK; Met Office, Exeter,

ABSTRACT

In order to explore the effects of climate change on atmospheric convection and the water cycle, we develop and analyse an extension of the Rainy-Bénard model, which is itself a moist version of the Rayleigh-Bénard model of dry convection. Including moisture changes the character of the convection, with condensation providing a source of buoyancy via latent heating and the system exhibiting moist conditional instability. A range of idealised climate change scenarios are constructed by appropriate choice of both the radiative cooling rate and the surface temperature, and these scenarios are investigated over a wide range of surface relative humidity values. We impose moist-pseudoadiabatic conditions at the top boundary. which allow the temperature and specific humidity values to vary at the top boundary in response to convection. The model is analysed across the different climate change scenarios space by examining diagnostics of the model's basic state, and its stability, with Convective Available Potential Energy (CAPE) calculations and a linear stability analysis. We use the linear stability results to identify new parameters relevant for this moist convective system, and to understand how the linear instability responds to the climate parameters. In particular, we define the "Rainy number" as a scaled ratio of positive-area CAPE and diffusion parameters. An alternative radiative-based Rainy number also is shown to describe the parameter space, especially for problems relating to changes in flux conditions. The Rainy number acts like the traditional Rayleigh number for dry Rayleigh-Bénard convection, and provides a novel theoretical tool for understanding how the dynamics and scales of moist convection and hence precipitation will change under climate change. The linear analysis predicts an intensification of the hydrological cycle under climate change. The model set up and linear analysis provide a basis for future investigation into the non-linear dynamics of (idealised) moist convection.

ARTICLE HISTORY

Received 2 February 2025 Accepted 31 August 2025

KEYWORDS

Moist convection: climate change; precipitation; linear stability analysis

1. Introduction

The Rainy-Bénard model (Vallis et al. 2019) is a moist extension of dry Rayleigh-Bénard convection. The Rainy-Bénard model is deliberately idealised, capturing some essential



ingredients of moist convection: (moist) conditional instability, latent heat release by condensation, energy and moisture budget constraints, and, a Clausius-Clapeyron relationship for the saturation vapor pressure with temperature; but missing more complex processes, such as liquid water or ice phases, or interactive radiative cooling schemes. The connection of Rainy-Bénard convection to classical Rayleigh-Bénard convection provides a suite of mathematical techniques that can be used to investigate the moist convective system. We aim to improve the theoretical understanding of moist convection, and convective rainfall in a changing climate, through the detailed analysis of a minimal model of moist convection.

The changes in atmospheric deep convection, and the character of its associated rainfall, are uncertain in future climate (O'Gorman 2015). Moist convection is a key source of uncertainty in climate model simulations, due to its small scale processes, and its feedback on large scale climate processes, such as the Hadley circulation (Tomassini and Yang 2022). Understanding changes in the intensity, structure and organisation of moist convection under climate change are key for improving climate model projections, which are pertinent tools for protecting vulnerable communities in the future. How moist convection changes under climate change is therefore a critically-important problem in climate research.

Changes in deep convection have been investigated using a range of approaches. One approach involves the use of ensemble data from global-scale General Circulation Models (GCMs), with energy and moisture budgets used to examine future rainfall change (Held and Soden 2006, Seager et al. 2010, Byrne and O'Gorman 2015). However there is a large uncertainty in modelled convective rainfall over the tropics, due to coarse resolutions $(\sim 50 \, \mathrm{km})$ which require subgrid-scale convective parametrisations (O'Gorman 2015). With the development of exascale computing, there have been significant advances in GCM resolution, with kilometre-scale (k-scale) models now being able to explicitly resolve convection on global domains (Schär et al. 2020). Recently such models have been used in the study of rainfall change (Cheng et al. 2022). However moist biases have been found in studies of global convection-permitting models (CPMs), potentially due to these models not capturing key convective processes such as turbulence (Tomassini et al. 2023). Initial k-scale studies indicate that there still remain gaps in our understanding of atmospheric moist convection, some of which can be investigated using idealised studies which can resolve turbulence (Guichard and Couvreux 2017).

An alternative to global-scale modelling involves using CRMs (Cloud Resolving Models) or LES (Large Eddy Simulations) to resolve explicitly convective clouds, and their associated transient motions on smaller domains. Both GCMs and CRMs are dynamically based on an approximation of the Navier-Stokes equations, called the "primitive equations" (Phillips 1966), CRMs typically have higher resolutions (10 m-1 km) than GCMs. Although CRMs can marginally resolve convection, complexity arises in these models by the choice of the parametrisations used for the subgrid-scale (i) turbulent motions, (ii) microphysical processes, and (iii) radiative processes (Guichard and Couvreux 2017). The inherent complexity of GCMs, CRMs and LES makes understanding the dynamics of moist convection challenging, which has lead to a renewed interest in understanding these dynamics from a fluid dynamics point of view, using idealised models, such as the Rainy-Bénard model (Vallis et al. 2019, Oishi and Brown 2024, Agasthya et al. 2025).

The Rainy-Bénard model was introduced in Vallis et al. (2019) as an idealised model of moist convection. Vallis et al. (2019) derived the model equations, and explored the model's behaviour, through a brief linear analysis, and some non-linear simulation results. To further the understanding of the Rainy-Bénard model, Oishi and Brown (2024) conducted a detailed linear analysis, examining the basic state, onset of convection, eigenvalue spectra and eigenvector structure, all for a range of different model parameters. Agasthya et al. (2025) extended the Rainy-Bénard model to include a constant radiative cooling rate. Inspired by the study of Robe and Emanuel (1996), they presented a set of nonlinear simulation results for different radiative cooling rates, examining different moist convective scalings with the radiative cooling rate (such as the mass flux). They found that the Rainy-Bénard model produces similar moist convective scalings as those observed in more complex CRMs, highlighting the model's relevance to the study of atmospheric moist convection. The simplicity of the Rainy-Bénard model makes a detailed mathematical approach for understanding moist convection possible (Oishi and Brown 2024), which is unavailable to more complex models of moist atmospheric convection.

In the present paper, we aim first to document well-posed (idealised) climate change scenarios in Rainy-Bénard convection. The scenarios are constructed to relate to the radiative convective equilibrium experiments conducted in Wing et al. (2018). To study climate change we extend the Rainy-Bénard model by adding a constant radiative cooling term, as in Agasthya et al. (2025). By careful choice of both the radiative cooling rate and the surface temperature, we set up a range of climate change scenarios. We impose moist pseudoadiabatic boundary conditions at the top boundary, which gives the temperature and specific humidity freedom to adjust. We use a detailed linear analysis, similar to that of Oishi and Brown (2024), to understand how the fundamental (linear) behaviour of the model changes with the climate parameters. The simplicity of the model, the radiation term and uniform boundary conditions therein allow us to establish a theoretical framework required for a conceptual approach to the climate change problem, based on fundamental principles of fluid dynamics. In particular, we will link a wider range of moist, radiatively cooled regimes, to understand the underlying mathematical behaviour of our climate change scenarios.

Convection is in general characterised by highly non-linear behaviour. However, linear theory has been used to understand the non-linear regimes of classical dry Rayleigh-Benard convection (Christopher et al. 2023), and therefore, we perform a linear analysis of the (moist) Rainy-Bénard model to gain an initial insight of the behaviour underpinning the non-linear regimes of the model. The study by Agasthya et al. (2025) used non-linear simulations of radiatively cooled Rainy-Bénard convection, finding similar scalings to those found in previous CRM studies, indicating that the Rainy-Bénard model can provide relevant results despite its simplicity. A linear analysis of the Rainy-Beńard model has been conducted in the Oishi and Brown (2024) study, which examined the convective onset (critical Rayleigh number), convective instability and moist internal gravity waves for the Rainy-Beńard model. We present a similar linear analysis here, however we use alternative boundary conditions and include a radiative cooling term as required for a climate change study. We also conduct a more detailed analytical treatment of the basic state solution, use a different approach to solving the linear stability eigenvalue problem, provide a different dispersion relationship for the (linear) internal gravity waves, and use conditional instability and moisture diagnostics to interpret the results.

In dry Rayleigh-Benard convection, some insight into the non-linear problem for higher Rayleigh numbers can be obtained from studying criticality. Malkus (1981) argues that dry convection acts to modify mean states to marginality, underlining the importance

of understanding such states. However, at higher Rayleigh numbers, turbulence acts not only to modify the mean state but also to cascade energy to smaller scales (Marston and Tobias 2023). The linear results presented in this paper provide the basis for a future investigation into the non-linear behaviour of moist convection under climate change, as has been successfully demonstrated for the "dry" classical Rayleigh-Beńard problem over many years (Chandrasekhar 1961, Malkus 1981, Yano 2023).

The paper starts with setting up the Rainy-Bénard model for a climate change study, discussing boundary conditions, radiative cooling, different non-dimensionalisations and key parameters (section 2). The analytical basic state solution is calculated across the climate parameter space, then some key diagnostics are presented (section 3). We then analyse the stability of the basic state and its dependence on the climate parameters, using (i) CAPE calculations and (ii) a linear stability analysis (section 4). The main findings and future research involving non-linear simulations are discussed in the conclusion (section 5).

2. Model set up for climate-forcing simulations

We use a radiatively extended Rainy-Benard model for this study. The Rainy-Bénard model is a moist extension of the Rayleigh-Bénard model, which uses the Boussinesq approximation. The moist extension is imposed by adding additional equations to the dry model for the specific humidity (q) and saturated specific humidity (q_s) , which are coupled to the buoyancy equation through a condensation term. As in Vallis et al. (2019), we consider the perturbation temperature, $\delta T = T - T_0$ about a constant reference temperature $T_0=300$ K. The potential temperature is given by $\theta=\theta_0+\delta\theta=T-gz/c_p$ (where $\theta_0 = T_0 = 300 \,\mathrm{K}$), and the buoyancy is given by $b = g \delta\theta/\theta_0$. The buoyancy equation differs from dry Rayleigh-Bénard convection in the inclusion of a condensation term, $C \equiv \gamma (q - q_s) \mathcal{H}(q - q_s) / \tau$ (Vallis et al. 2019), and has been extended here for climate study with a constant radiative cooling term, gr/θ_0 , where r is the radiative cooling rate. Condensation also provides a sink in the specific humidity equation. The inclusion of a constant radiative cooling term in the buoyancy equation gives the same model equations as those in Agasthya et al. (2025), but different boundary conditions are applied. The model set up differs from Oishi and Brown (2024) and Vallis et al. (2019) both in the inclusion of radiative cooling, and in the choice of the boundary conditions. The Boussinesq, radiative moist convective system is given by,

$$\frac{D\mathbf{u}}{Dt} = -\nabla\phi + b\mathbf{k} + \nu\nabla^2\mathbf{u},\tag{1}$$

$$\frac{Db}{Dt} = \gamma \frac{q - q_s}{\tau} \mathcal{H}(q - q_s) + \kappa \nabla^2 b - \frac{g}{\theta_0} r, \tag{2}$$

$$\frac{Dq}{Dt} = -\frac{q - q_s}{\tau} \mathcal{H}(q - q_s) + \kappa_q \nabla^2 q,$$
(3)

$$\delta T = \frac{\theta_0}{g}b - \frac{g}{c_p}z,\tag{4}$$

$$q_s = q_0 e^{\alpha \delta T},\tag{5}$$

$$\nabla \cdot \mathbf{u} = 0. \tag{6}$$

As in Vallis et al. (2019), $\gamma = gL/(c_p\theta_0)$ and $\alpha = L/(R_vT_0^2) - c_p/(R_dT_0)$, where L is the latent heat of condensation, c_D is the specific heat capacity of air at constant pressure, R_d is the gas constant for dry air, and, R_{ν} is the gas constant for water vapor. Equation (5) is the Clausius-Clapeyron relation (5), linearised about T_0 . The model has simple microphysics: no liquid water or ice phases are included, and condensation is idealised as a relaxation process. We note that an alternative approach for formulating the multiphase moist convective system could be pursued by building on the work by Busse and Schubert (1971). Radiation is also idealised as a constant cooling rate, r, which provides a first-order approximation of the radiative cooling in the atmosphere (Jeevanjee and Fueglistaler 2020, Agasthya et al. 2025). The simplicity of the radiative cooling and microphysics makes a detailed fundamental analysis of the model possible.

2.1. Boundary conditions

We set up idealised climate change scenarios by careful choice of the boundary conditions, as well as the radiative cooling rate. We take the surface boundary conditions to be

$$b(0) = g\Delta T_{\text{surf}}/\theta_0, \quad q(0) = RH_{\text{surf}} q_s(0) = RH_{\text{surf}} q_0 e^{\alpha \Delta T_{\text{surf}}}, \quad \mathbf{u}(0) = \mathbf{0}.$$
 (7)

We impose a surface temperature of $T = T_0 + \Delta T_{\text{surf}}$ and a surface relative humidity, where the relative humidity is defined as $RH \equiv q/q_s$. We use equation (4) to define b(0), and equation (5) to define q(0). We also use idealised no-slip boundary conditions, at both boundaries (as in Vallis et al. 2019).

We use a simple "explicit" approach to change the surface temperature; we keep the reference temperature and potential temperature constant ($T_0 = \theta_0 = 300 \,\mathrm{K}$), modifying the temperature perturbation at the surface ($\delta T(0) = \Delta T_{\text{surf}}$) to change the surface temperature. We discuss an alternative "implicit" approach for imposing the surface temperature in Appendix A, which involves changing the surface temperature by modifying the reference temperature and potential temperature directly ($T_0 = \theta_0 = 300 \text{ K} + \Delta T_{\text{surf}}$, which in turn modifies the values of the parameters q_0 , $\alpha \& \gamma$), whilst keeping $\delta T(0) = 0$. The explicit approach is easier to interpret and implement than the implicit method (see Appendix A), whilst still capturing the key aspects associated with altering the surface temperature, and therefore we use the explicit method in the rest of the analysis.

The top of the domain represents the tropopause. We use moist pseudoadiabatic boundary conditions at the top boundary, which can be expressed as,

$$\frac{\mathrm{d}m}{\mathrm{d}z}(H) = \frac{\mathrm{d}b}{\mathrm{d}z}(H) + \gamma \frac{\mathrm{d}q}{\mathrm{d}z}(H) = 0, \quad q(H) = q_s(H), \quad \mathbf{u}(H) = \mathbf{0}. \tag{8}$$

Note that $m = b + \gamma q$ is the moist static energy of the model, and the moist pseudoadiabat is defined as a profile for which dm/dz = 0 and $q = q_s$ (Vallis et al. 2019). Imposing moist pseudoadiabatic boundary conditions allows the temperature and moisture to adjust to moist convection. In Vallis et al. (2019), Oishi and Brown (2024) and Agasthya et al. (2025), both T(H) and q(H) were fixed, so there was no possibility to adjust the upper levels to a convectively controlled profile, and the stratification leads to an unrealistic downward heat flux. In the real atmosphere, the diffusive fluxes of buoyancy and humidity $(\kappa \partial b/\partial z, \kappa_q \partial q/\partial z)$ are small at the tropopause, and the profile is close to the moist pseudoadiabat, especially in the tropics. The top boundary conditions are consistent with atmospheric conditions at the tropopause, and they additionally allow convective adjustment of the profiles.

2.2. Idealised climate change scenarios

We set up the control climate to be an atmosphere with surface temperature $T(0) = 300 \, \text{K}$, and a constant radiative cooling rate of $r = 1.5 \, \text{K/day}$. Idealised climate change scenarios are set up by careful choice of both the radiative cooling rate and the surface temperature. We consider three distinct values of the surface temperature, and for each of these surface temperatures, consider three different radiative cooling rates, corresponding to eight scenarios differing from the control climate:

$$(\Delta T_{\text{surf}}, r)$$
 where $\Delta T_{\text{surf}} \in \{0, 5, 10\} \text{ K}, r \in \{1.5, 3, 6\} \text{ K/day}.$

For each pair of surface temperature and radiative cooling, ($\Delta T_{\rm surf}, r$), we consider a wide range of values for the surface relative humidity ($RH_{\rm surf} \in [0.20, 0.99]$). To define the climate change scenarios, we impose larger surface temperatures than the control climate ($\Delta T_{\rm surf} = 5 {\rm or} 10 \, {\rm K}$). The radiative cooling rate of the atmosphere is sensitive to the value of the surface temperature, relative humidity, and the lapse rate of the atmosphere (Jeevanjee and Fueglistaler 2020, Hartmann *et al.* 2022), and hence we consider a range of different combinations of surface temperature and radiative cooling rates in our different climate change scenarios. Typically, larger surface temperatures are associated with larger radiative cooling rates (e.g. Figure 4 of Jeevanjee and Fueglistaler 2020), and so we define our "typical" climate change scenario as moving from the control climate to a climate with $T(0) = 310 \, {\rm K} \, (\Delta T_{\rm surf} = 10 \, {\rm K})$ and $r = 3 \, {\rm K/day}$, with the surface relative humidity held constant.

2.3. Dry adiabatic buoyancy non-dimensionalisation

Following Appendix 7.1 in Vallis *et al.* (2019), we use a "buoyancy based non-dimensionalisation". We cannot use the classical Rayleigh-Bénard temperature scale [T] = T(0) - T(H), since T(H) is free to adjust to moist convection under our moist pseudoadiabtic boundary conditions specified in section 2.1. The temperature scale is instead set by the dry adiabatic temperature difference, $[T] = T_d(0) - T_d(H) = gH/c_P \sim 100 \text{ K}$.

We use equation (4) to set the buoyancy scale to be proportional to the temperature scale, $[B] = g[T]/\theta_0 \sim 3.3 \text{ ms}^{-2}$. The length scale is defined to be height of the domain, $[L] = H \sim 10 \text{ km}$, and we define the timescale using $[t] = ([L]/[b])^{1/2} \sim 55 \text{ s}$. We scale the specific humidity by $[q] = q_0 \sim 3.8 \times 10^{-3}$ which is lower than its real value (see Appendix D), to ensure that the fluxes of buoyancy and humidity are small at the top boundary. The velocity scale is set by $[U] = [L]/[t] \sim 180 \text{ ms}^{-1}$ and the pressure scale by $[\phi] = [U]^2 \sim 3.3 \times 10^5 \text{ Pa}$. The non-dimensional system is then given by,

$$\frac{D\hat{\mathbf{u}}}{D\hat{t}} = -\hat{\nabla}\hat{\phi} + \hat{b}\mathbf{k} + \left(\frac{Pr}{Ra}\right)^{\frac{1}{2}}\hat{\nabla}^2\hat{u},\tag{9}$$

$$\frac{D\hat{b}}{D\hat{t}} = \hat{\gamma} \, \frac{\hat{q} - \hat{q_s}}{\hat{\tau}} \mathcal{H}(\hat{q} - \hat{q_s}) + \frac{1}{(PrRa)^{\frac{1}{2}}} \hat{\nabla}^2 \hat{b} - \hat{r}, \tag{10}$$

$$\frac{D\hat{q}}{D\hat{t}} = -\frac{\hat{q} - \hat{q}_s}{\hat{\tau}} \mathcal{H}(\hat{q} - \hat{q}_s) + \frac{S_m}{(PrRa)^{\frac{1}{2}}} \hat{\nabla}^2 \hat{q}, \tag{11}$$

$$\hat{\nabla} \cdot \hat{\mathbf{u}} = 0, \tag{12}$$

$$\hat{\delta T} = \hat{b} - \hat{z},\tag{13}$$

$$\hat{q}_s = e^{\hat{\alpha}\hat{\delta}T}.\tag{14}$$

Here we have the non-dimensional parameters

$$Pr = \frac{v}{\kappa}, \quad Ra = \frac{g^2 H^4}{\theta_0 c_p v \kappa}, \quad \hat{\gamma} = \frac{\gamma q_0 \theta_0 c_p}{g^2 H}, \quad \hat{\tau} = \frac{\tau g}{(c_p \theta_0)^{1/2}}$$
(15)

$$\hat{r} = \frac{(c_p^3 \theta_0)^{1/2} r}{g^2 H}, \quad S_m = \frac{\kappa_q}{\kappa}, \quad \hat{\alpha} = \frac{g H \alpha}{c_p}, \quad \hat{b}_{\text{surf}} = \frac{c_p \Delta T_{\text{surf}}}{g H}.$$
 (16)

We take $Pr = S_m = 1$, $\hat{\gamma} = 0.25$, $\hat{\alpha} = 6.0$ and $\hat{\tau} = 0.05$ (corresponding to a condensational timescale of $\tau \sim 1s$, which is small to keep the supersaturation low). We vary the parameters \hat{r} , \hat{b}_{surf} and Ra. Note that $\hat{r} = 1 \times 10^{-5}$ for a typical atmospheric cooling rate of 1.5 Kday⁻¹, and $\hat{b}_{\text{surf}} = 0.05$ for a surface temperature 5 K warmer than the reference temperature ($T_0 = 300 \text{ K}$). For molecular values of κ and ν , $Ra \sim 10^{23}$.

The dry adiabatic temperature and buoyancy scales used in this non-dimensionalisation do not reflect changes in stability caused by changes in the temperature profile via changes in surface temperature, surface moisture, or ultimately, radiative cooling. Therefore Ra in this non-dimensionalisation is only sensitive to changes in κ or ν . However, the dry adiabatic buoyancy non-dimensionalisation simplifies the form of the equations, and allows easy implementation of the climate change scenario, and we therefore employ the dry adiabatic buoyancy non-dimensionalisation in the rest of the analysis in this paper. Note that we drop the hats on the parameters for the rest of the analysis.

2.4. Integral constraints: energy and moisture budgets

By integrating the moisture and buoyancy equations over the atmospheric column, we can obtain integral constraints on the model. This approach is well understood in climate science and is one basis for analysing future rainfall patterns (Held and Soden 2006, Byrne and O'Gorman 2015). We consider these constraints for equilibrium, in which $\partial/\partial t = 0$. Using equation (11), we can write the water budget (column integrated moisture equation) as,

$$\int_0^1 \left(Ra^{-1/2} \nabla^2 q - \nabla \cdot (\boldsymbol{u}q) \right) \, \mathrm{d}z = \int_{q > q_s} \frac{q - q_s}{\tau} \, \mathrm{d}z \equiv P, \tag{17}$$

where we have defined the precipitation term (*P*) to be the column integral of the moisture sink associated with condensation, with condensation defined as,

$$C \equiv \gamma \, \frac{q - q_s}{\tau} \mathcal{H}(q - q_s).$$

Similarly, the energy budget (column integrated buoyancy equation) can be written as,

$$r - \int_0^1 \left(Ra^{-1/2} \nabla^2 b - \nabla \cdot (\boldsymbol{u}b) \right) \, \mathrm{d}z = \gamma \int_{q > q_s} \frac{q - q_s}{\tau} \, \mathrm{d}z = \gamma P. \tag{18}$$

It is common in climate change studies to separate the horizontal and vertical components of the budgets. We define the (diffusive) evaporation as,

$$E \equiv -Ra^{-1/2} \left(\frac{\partial q}{\partial z} \bigg|_{z=0} - \left. \frac{\partial q}{\partial z} \right|_{z=1} \right),$$

i.e. the sum of the moisture source at the bottom boundary, and the moisture sink at the top boundary, due to diffusion. We also define the (diffusive) sensible heat flux as,

$$F_{\mathsf{sh}} \equiv -Ra^{-1/2} \left(\frac{\partial T}{\partial z} \bigg|_{z=0} - \left. \frac{\partial T}{\partial z} \right|_{z=1} \right) = -Ra^{-1/2} \left(\left. \frac{\partial b}{\partial z} \right|_{z=0} - \left. \frac{\partial b}{\partial z} \right|_{z=1} \right).$$

Equations (17) & (18) can then be written as,

$$P = E + \int_0^1 \left(Ra^{-1/2} \nabla_h^2 q - \nabla_h \cdot (\boldsymbol{u}q) \right) \, \mathrm{d}z, \tag{19}$$

$$\gamma P = r - F_{\mathsf{sh}} - \int_0^1 \left(Ra^{-1/2} \nabla_h^2 b - \nabla_h \cdot (\boldsymbol{u}b) \right) dz. \tag{20}$$

By integrating equations (19) & (20) in the horizontal, and applying the divergence theorem and periodic horizontal boundary conditions, the domain averaged budgets simplify to

$$\overline{P} = \overline{E},$$
 (21)

$$r = \gamma \, \overline{P} + \overline{F_{\mathsf{sh}}},\tag{22}$$

where $\overline{}$ denotes the horizontal average of a quantity. The simplified water budget implies that the precipitation (moisture sink) is balanced by the evaporation (moisture source from diffusion), whilst the energy budget implies that the radiative cooling is balanced by the sum of heating associated with the precipitation (γP) and the sensible heat flux (heat source from diffusion). Assuming the fluxes of buoyancy and moisture are small at the top of the domain (relative to the surface fluxes), the energy budget (approximately) relates the radiative cooling to the surface fluxes:

$$r \approx \gamma \, \overline{E}_{\text{surf}} + \overline{F}_{\text{ssh}},$$
 (23)

Where $E_{\text{surf}} = -Ra^{-1/2}\partial q/\partial z(z=0)$ is the surface evaporation, and $F_{\text{ssh}} = -Ra^{-1/2}\partial T/\partial z(z=0)$ is the surface sensible heat flux.

Note that, as $Ra \to \infty$, $E, F_{sh} \to 0$, so equation (21) $\Rightarrow P \to 0$, and the simplified energy budget equation (22) becomes inconsistent unless $r \to 0$ as $Ra \to \infty$, indicating that (steady) equilibrium cannot exist in this limit.



2.5. Moist stability

To understand the moist stability of the atmosphere, it is typical in atmospheric science and meteorology to use a parcel argument (Vallis 2017). Consider a moist parcel of air. In the absence of diffusion, radiative cooling and condensation, the moist static energy of the parcel is conserved (Dm/Dt = 0). If the parcel of air is unsaturated $(q < q_s)$, we rise the parcel along the dry adiabat (where db/dz = 0, so b is conserved) also conserving the humidity of the parcel (equation (11) for $q < q_s$ and no diffusion), until the parcel becomes saturated at the (parcel) lifting condensation level (LCL), where $q = q_s$. We then rise the now saturated parcel along the moist pseudoadiabat, where m is conserved and $q = q_s(T)$. The moist pseudoadiabatic buoyancy and temperature profiles of the atmospheric parcel (and the moist adiabatic lapse rate, $\Gamma_m = -dT_m/dz$) can be determined by solving the equation $m = b(T) + \gamma q(T) = m(0)$ as a function of height.

We define the buoyancy and temperature of parcel using b_p and T_p respectively, and that of the environment with b_E and T_E . In the absence of diffusion, an environmental profile can be defined as absolutely unstable, if the parcel satisfies $T_p \geq T_E \Rightarrow b_p \geq b_E$ at each height, z. In this case, the air parcel would be more buoyant (warmer) than its environment everywhere, and so would rise (or convect) freely. If instead the parcel is less buoyant (cooler) than its environment up to a height z = LFC < H, and more buoyant (warmer) than its environment for LFC $\leq z \leq LNB$, we can describe the atmosphere as conditionally unstable: for the parcel to convect freely (up to z = LNB, the level of neutral buoyancy, which is defined to be above the LFC), the parcel must be lifted (through turbulent or mechanical lifting) to the level of free convection (LFC). If the parcel is less buoyant (cooler) than its environment ($T_p \leq T_E \Rightarrow b_p \leq b_E$) at all heights z, the environment is absolutely stable. Note that conditional stability of a profile is no longer a local measure, because finite amplitude displacements may be needed to rise a parcel above its LFC in order to release energy. An example of a conditionally unstable (basic state) environment is shown in figure 1.

To quantify the conditional instability of the environment, we use Convective Available Potential Energy (CAPE). Figure 1 shows a schematic of how CAPE is calculated. The area of the orange region in figure 1 is the convective inhibition (CIN), where the parcel is less buoyant than its environment. Above the LFC, the area of the blue region is the positive CAPE (pCAPE), where the parcel is more buoyant than its environment. We additionally define (net) CAPE = $\int_0^H (b_p - b_{BS}) dz = pCAPE - CIN$. The positive CAPE can be thought of as the total amount of energy that can be released (by convection) in the system, and according to the parcel argument, positive CAPE is a necessary condition for the system to be able to release energy. However it does not tell us about convective onset in the system, i.e. when the system will overcome diffusion, which is determined by a linear stability analysis.

Several alternatives to CAPE for quantifying conditional instability have been proposed in the literature (Randall and Wang 1992, Tailleux and Grandpeix 2004, Yano *et al.* 2005). For example, Yano *et al.* (2005) introduces potential energy convertibility (PEC) as "a further generalisation of CAPE". PEC builds on the cloud work function introduced in Arakawa and Schubert (1974). The calculation of PEC is more involved than that of CAPE, as it requires a general profile of vertical velocity. For the stability of the basic state considered in this paper, u = w = 0 and so PEC cannot be defined and therefore cannot be used

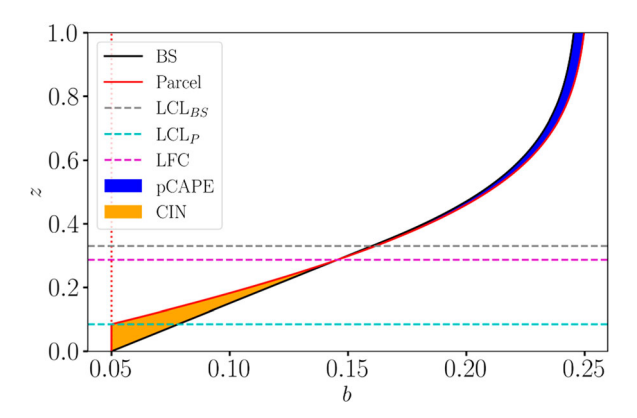


Figure 1. CAPE calculation schematic. The black line shows the basic state (BS) buoyancy curve, with the grey dashed line marking the basic state LCL. The red line marks the buoyancy profile of a parcel (P), the dashed cyan line marks the LCL of the parcel, and the dashed magenta line corresponds to the LFC, where the buoyancy of the parcel and the basic state are equal. Note that the LNB, where the buoyancy of the parcel and the basic state become equal again, is higher than the domain height. The area of the blue shaded region is the positive CAPE, and the area of the orange shaded region gives the CIN. (Colour online).

to quantify the conditional instability in our system. Tailleux and Grandpeix (2004) discuss the idea of moist available energy (MAE) which is reliant on defining an appropriate reference state for the system which minimises the enthalpy of the system. MAE is complex to compute, and does not have an obvious equivalent energy barrier like CIN in the computation of CAPE. Although CAPE has its limitations, it does measure conditional instability without reference to a velocity profile, and is used widely in the climate community, including in idealised modelling studies (Muller *et al.* 2011, Singh and O'Gorman 2013, Muller and Takayabu 2020), so we retain it here.

In dry Rayleigh-Bénard convection, the system is dry unstable (db/dz < 0) assuming the top plate is cooler than the bottom plate $(T_1 < T_0)$. It is typical to quantify the dry instability by the temperature difference across the domain; we show in Appendix B that the temperature difference is proportional to CAPE in the dry system. Just as the dry Rayleigh number is a ratio of dry instability (quantified by the temperature difference across the domain) to the diffusion in the model, we argue that a Rayleigh number for the moist system should represent a measure of the conditional instability to the diffusion in the model.

2.6. Non-dimensionalisations for conditionally unstable atmospheres

The buoyancy non-dimensionalisation introduced in Vallis *et al.* (2019) scales buoyancy with $[B] = g\Delta T/c_p$, where $\Delta T = T(0) - T(H)$. The boundary conditions on temperature (or buoyancy) and humidity were fixed at both the top and bottom boundaries in the Vallis *et al.* (2019) study, so the temperature difference can be chosen independently of the humidity, as an external parameter. The temperature difference associated with our conditionally unstable (basic state) environments is always stable to dry air motion (db/dz > 0 or b(H) > b(0)). Therefore this measure of buoyancy relates to the stabilising

effects of warming of air as it descends with constant b. It has no dependence on the moisture in the system, and therefore it does not capture any changes in instability associated with variations in moist convective conditions. In the conditionally unstable system, instabilities are instead driven by the buoyancy of saturated air parcels rising above their LFC. We present two different scalings for [B] (and [L]) which are more appropriate for (moist) conditionally unstable atmospheres.

2.6.1. Bretherton non-dimensionalisation

Bretherton (1988) introduced a moist Rayleigh number that captures some effects of conditional instability. Though his model differs from the Rainy-Bénard model (see Bretherton 1987 for further details), the moist Rayleigh number can be simply calculated for our system. Bretherton (1988) defined the moist Rayleigh number as,

$$Ra_m = N_m^2 = \frac{H^4(\Gamma - N_d^2)}{\pi^4 v^2}$$

Where $N_d^2 = (b_E(H) - b_E(0))/H$ is the Brunt-Vaisala frequency of the environment, and $\Gamma \approx (b_p(H) - b_p(0))/H$ is "the buoyancy generation per unit rise due to latent heating" in "the (saturated) adiabatic ascent of a moist air parcel". Note that the moist Rayleigh number is identified as an eigenvalue in Bretherton (1987), however it is not an eigenvalue of the current system. The Bretherton (1988) study uses the conditions $N_d^2 > 0 \Rightarrow$ $b_E(H) > b_E(0)$ and $\Gamma > N_d^2 \Rightarrow b_p(H) > b_E(H)$ to define a conditionally unstable atmosphere. For our model, we can define the moist "Bretherton" Rayleigh number (Ra_m) by setting [L] = H, $[B] = b_p(H) - b_e(H)$, $[t] = \sqrt{[L]/[B]}$, which leads to the expression,

$$Ra_{m} = \frac{H^{3}(b_{p}(H) - b_{E}(H))}{\kappa \nu}.$$
 (24)

The expression of Ra_m given in equation (24) captures the ratio of conditional instability (quantified by the buoyancy difference between a parcel and its environment at z = H) to diffusion. However, the simple buoyancy scale ($[B] = b_p(H) - b_E(H)$) does not account for the curvature of the environmental and buoyancy profiles as shown in figure 1. For this reason, we here introduce a non-dimensionalisation based on the pCAPE of the environment, which provides an alternative (more accurate) measure of the conditional instability of the environment.

2.6.2. pCAPE non-dimensionalisation

For a given set of boundary conditions, we first calculate the parcel buoyancy (or temperature) profile. Based on the environmental buoyancy (or temperature) profile, we can then calculate the pCAPE of the environment, which we use as a scale for the kinetic energy in the model, so that $[U] \sim \sqrt{\text{pCAPE}}$. Assuming that $b_p \geq b_e$ for LFC $\leq z \leq$ LNB, we take the (CAPE) length scale to be [L] = LNB - LFC, which determines the buoyancy scale $([B] \sim [U]^2/[L])$ and timescale $([t] \sim [U]/[L])$ for the system. Note that for the environment shown in figure 1, we set LNB = H, i.e. the domain height. The scales associated with this non-dimensionalisation are:

$$[U] = \sqrt{\text{pCAPE}}, \quad [B] = \frac{\text{pCAPE}}{\text{LNB} - \text{LFC}}, \quad [L] = \text{LNB} - \text{LFC}, \quad [t] = \frac{\text{LNB} - \text{LFC}}{\sqrt{\text{pCAPE}}}.$$
(25)

Additionally, we set the pressure scale to be $[\Phi] = [U]^2 = pCAPE$. The non-dimensional momentum equation is then given by,

$$\frac{D\mathbf{u}}{Dt} = -\nabla\phi + b\mathbf{k} + \left(\frac{Pr}{Ry}\right)^{\frac{1}{2}}\nabla^2\mathbf{u},\tag{26}$$

where,

$$Ry \equiv \frac{\text{pCAPE} \times (\text{LNB} - \text{LFC})^2}{\nu \kappa}$$
 (27)

is the "Rainy" number, which is a moist version of the Rayleigh number.

The Rainy number represents the ratio of the destabilising effect of conditional instability (quantified by CAPE) to the stabilising effect of diffusion in the model, and therefore more faithfully corresponds to the role of Rayleigh number in dry classical Rayleigh-Bénard convection. The Bretherton (1987) study identified a moist Rayleigh number of a similar form (measuring conditional instability against diffusion) as an eigenvalue of their moist convective system, which further supports the suitability of a Rainy number constructed using the above quantification. Figure 2 shows the critical "classical" Rayleigh number, the critical moist Bretherton Rayleigh number, the critical Rainy number and the critical radiative Rainy number across the (b_{surf}, r) parameter space, as calculated by a linear stability analysis. Note that the linear stability analysis is discussed in detail in section 4. The Rainy number varies much less than the "classical" (dry) critical Rayleigh number over the parameter space, as a result of including a measure of moist instability in the definition of the Rainy number. Additionally, the Rainy number varies less than the moist "Bretherton" Rayleigh number across the parameter space as a result of choosing CAPE (instead of $b_p(H) - b_E(H)$) to quantify conditional instability. The results in figure 2 therefore show that Ry is more useful than Ra_d and Ra_m in categorising the behaviour of the moist conditionally unstable system. We need to know the basic state to be able to compute CAPE and hence Ry, however calculating CAPE is routine in meteorology and climate studies.

We derive the radiative Rainy number (shown in the lower right panel) in Appendix C, by using the surface flux of moist static energy as an alternative measure of conditional instability in the system. By quantifying the surface flux of *m*, the radiative Rainy number becomes relevant for climate studies focussed on the response of moist convection to different surface fluxes. The CAPE based Rainy number given by equation (27) can be used to understand the water cycle intensification under climate change (observed previously in Kendon *et al.* (2019)).

3. Basic state analysis

To understand the behaviour of the model (under the dry adiabatic buoyancy non-dimensionalisation) with the boundary conditions specified in section 2.1, a natural starting point is to calculate the basic state. Pauluis and Schumacher (2010) examine steady

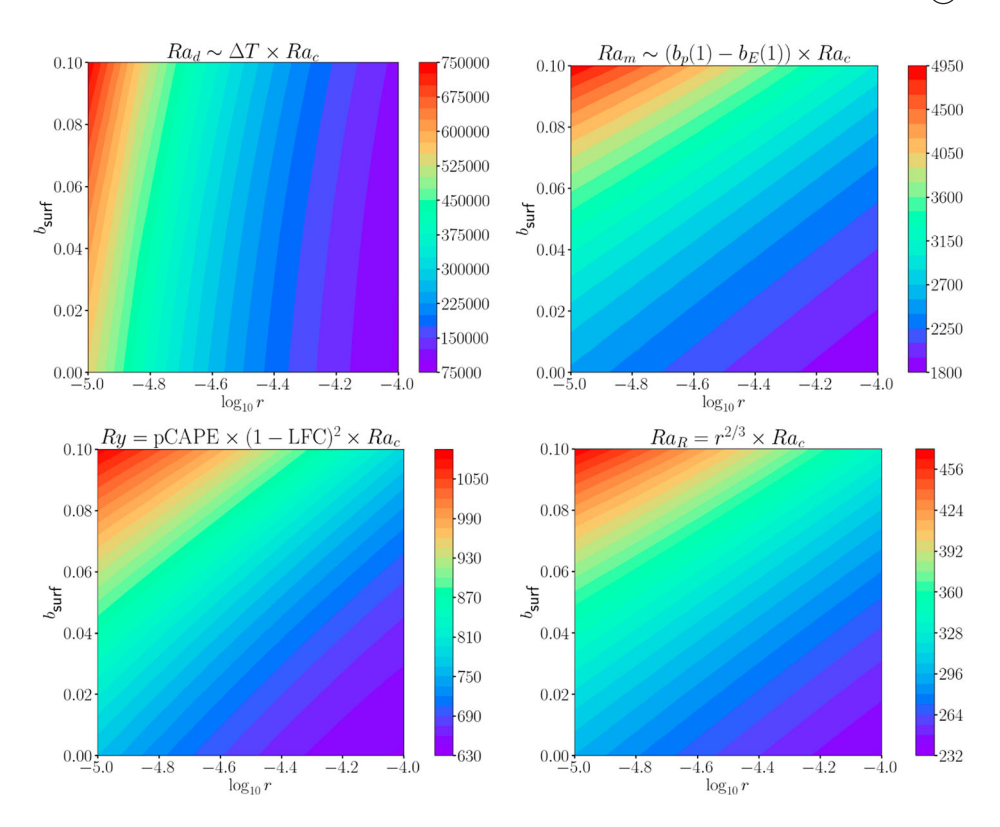


Figure 2. Critical dry Rayleigh number (top left), moist "Bretherton" Rayleigh number (top right), Rainy number (bottom left) and radiative Rainy Number (bottom right), as a function of the surface temperature and radiative cooling rate. The surface relative humidity is kept fixed at $RH_{surf} = 0.6$. The classical dry Rayleigh number shows variation of a factor of ~ 10 at criticality over the parameter space, while the moist "Bretherton" Rayleigh number varies by a factor of ~ 2.75 , the radiative Rainy number varies by a factor of ~ 1.75 . (Colour online)

state solutions to their simple model of moist convection, and in both Vallis *et al.* (2019) and Oishi and Brown (2024) a "drizzle solution" of no motion is found for fixed temperature conditions, and saturated upper and lower boundary conditions. Here, the problem is similar to that of Vallis *et al.* (2019) and Oishi and Brown (2024), although the analysis is conducted for the idealised climate change set up of the Rainy-Bénard model with radiation and moist pseudoadiabatic upper boundary conditions (outlined in section 2.1), and moreover the solution is here found analytically (as in Oishi and Brown 2024). Once the basic state solution is known, the stability of the system can be understood by calculating CAPE and the linear stability of the system (from the basic state).

The basic state we find is a z-dependent state of no motion ($\mathbf{u} = \mathbf{0}$), which is time-independent ($\partial/\partial t = 0$). For the boundary conditions outlined in section 2.1, the basic state solution consists of a lower unsaturated region with an upper saturated region. Dropping the hats, the basic state equations (for Pr = Sm = 1) are given by

$$\frac{\mathrm{d}\phi}{\mathrm{d}z} = b,\tag{28}$$

$$\frac{\mathrm{d}^2 b}{\mathrm{d}z^2} = Ra^{1/2} \left(-\gamma \frac{q - q_s}{\tau} \mathcal{H}(q - q_s) + r \right),\tag{29}$$

$$\frac{\mathrm{d}^2 q}{\mathrm{d}z^2} = Ra^{1/2} \frac{q - q_s}{\tau} \mathcal{H}(q - q_s),\tag{30}$$

$$q_s = e^{\alpha(b-z)}. (31)$$

We can combine the buoyancy and specific humidity ODEs to obtain the moist static energy equation,

$$\frac{d^{2}(b+\gamma q)}{dz^{2}} = \frac{d^{2}m}{dz^{2}} = Ra^{1/2}r.$$

Upon applying the boundary conditions in section 2.1, the buoyancy can be related to specific humidity throughout the domain by

$$m \equiv b + \gamma q = m_{\text{surf}} + Rz^2/2 - Rz, \tag{32}$$

where $R \equiv Ra^{1/2}r$. It follows that (31) can be written as

$$q_s(q, z) = \exp\left(\alpha(-\gamma q + m_{\text{surf}} + Rz^2/2 - (R+1)z)\right).$$
 (33)

The basic state solution can be determined by solving (30), where $q_s(q, z)$ is given by (33). Due to the non-linear Heaviside function \mathcal{H} , (30) must be solved separately in the unsaturated and saturated regions. These solutions are matched at the lifting condensation level (LCL) where $z = z_s$ and $q^* = q(z_s) = q_s(z_s)$. The matching conditions used at the LCL are continuity of b, q, and their first derivatives.

Since $\epsilon \equiv \tau / Ra^{1/2}$ is small, we use an asymptotic approach for this analysis (expanding $q = q_0 + \epsilon q_1 + \cdots$). In the unsaturated region, we solve

$$\frac{\mathrm{d}^2 q}{\mathrm{d}z^2} = 0 \quad \Rightarrow \quad \frac{\mathrm{d}^2 q_0}{\mathrm{d}z^2} + \epsilon \frac{\mathrm{d}^2 q_1}{\mathrm{d}z^2} \approx 0. \tag{34}$$

In the saturated region,

$$\frac{d^2q}{dz^2} = \frac{q - q_s}{\epsilon} \quad \Rightarrow \quad q_0 = q_s(q_0) \quad \& \quad q_1 = \frac{d^2q_0/dz^2}{1 + \alpha \gamma q_0},\tag{35}$$

where we have used a first order Taylor expansion about q_0 . The $\mathcal{O}(\epsilon)$ term is required to balance the diffusion of the $\mathcal{O}(1)$ solution. Note that the leading order solution has zero condensation and hence precipitation ($C(z) = 0 \Rightarrow P = 0$), since $q = q_s$ for $z \ge z_s$, and so we also need to consider the $\mathcal{O}(\epsilon)$ terms for the water budget equation (21) to be consistent. The analytical, asymptotic, basic state solution is given by $q = q_0 + \epsilon q_1 + \cdots$, where

$$q_0(z) = \begin{cases} q_{\text{surf}} + \left(\frac{q^* - q_{\text{surf}}}{z_s}\right) z, & \text{if } z < z_s \\ \frac{1}{\alpha \gamma} W\left(\alpha \gamma \exp\left\{\alpha \left(m_{\text{surf}} + \frac{R}{2} z^2 - (R+1)z\right)\right\}\right), & \text{if } z \ge z_s \end{cases}$$

and,

$$q_1(z) = \begin{cases} 0, & \text{if } z < z_s \\ \frac{\alpha q_0(z)}{(1 + \alpha \gamma \, q_0(z))^2} \left(R + \alpha \left\{ \frac{Rz - (R+1)}{1 + \alpha \gamma \, q_0(z)} \right\}^2 \right), & \text{if } z \ge z_s. \end{cases}$$

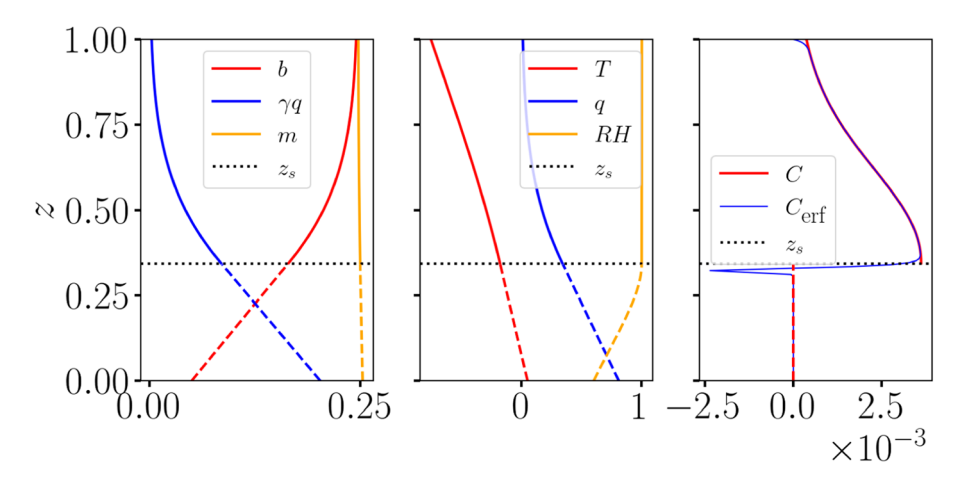
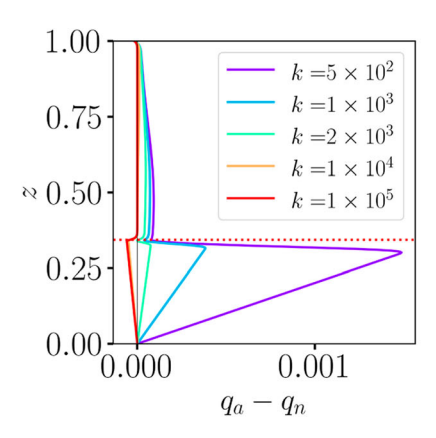


Figure 3. Analytical basic state solution profiles for $RH_{surf} = 0.6$, $b_{surf} = 0.05$ and $r = 1 \times 10^{-5}$. The unsaturated part of the solution is given by the dashed lines, and the saturated part is given by the solid lines. The numerical condensation profile (C_{erf}) for a smooth approximation of \mathcal{H} is also shown. (Colour online)

Here W is the Lambert-W function (the implicit solution of $W(x) \exp(W(x)) = x$ for any x). Note that the leading order solution above is the same as the analytical basic state solution presented in Oishi and Brown (2024); they find that the analytical (leading order) solution is close to the numerical solution of the NLBVP, provided the steepness of the smooth Heaviside approximation is large enough (see their figure 6). The higher order solution given by $q(z) = q_0(z) + \epsilon q_1(z)$ above produces a non-zero condensation term, which generally matches well when compared to the numerical NLBVP solution (where $\mathcal{H}(f) = \frac{1}{2}(1 + \operatorname{erf}(kf))$ with $k = 10^3$) as shown in figure 3.

The difference between the numerical and analytical basic state solutions is shown in figure 4, varying the Heaviside steepness (k) and resolution (nz). The discrepancy between the analytical and numerical solutions generally decreases with increasing k and nz, however the difference becomes nearly independent of the steepness and resolution, provided that they are large enough $(k \ge 1 \times 10^4, nz \ge 512)$. Note that there is always a difference between the numerical and analytical solutions, due to the continuous and discontinuous forms of \mathcal{H} used respectively (illustrated by the condensation profile in figure 3). We see that the moist pseudoadiabtic upper boundary conditions only hold to leading order: for the $q(1) = q_s(1)$ condition to hold in the $\mathcal{O}(\epsilon)$ solution, we require a boundary layer of $\mathcal{O}(\epsilon^{3/2})$, which is evident in the numerical profile of condensation in figure 3 and the right panel of figure 4.

Profiles of all other quantities can be deduced once q(z) is known, by additionally using the solution m(z) from equation (32). The profiles are shown for a specific set of climate parameters in figure 3. Each of the profiles in figure 3 show a lower unsaturated region (where $q < q_s$ or RH < 1), matched onto a saturated upper region (where $q \ge q_s$ or $RH \ge 1$), apart from the discontinuous condensation profile. Note that the basic state solution is saturated aloft, which differs from the real atmosphere, which is unsteady and nonlinear, but close to the moist pseudoadiabat with some conditional instability present. Figure 4 confirms how the upper profile is close to the moist pseudoadiabat, in contrast with Vallis



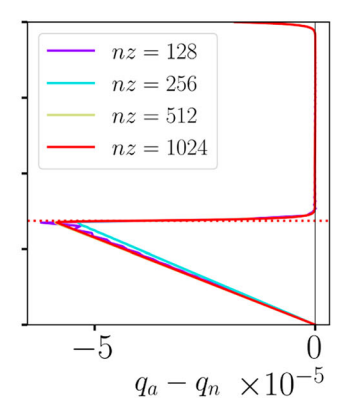


Figure 4. The difference between the analytical (q_a) and numerical (q_n) basic state solutions as a function of the Heaviside steepness (left), and, the vertical resolution (right). The dotted red line marks the LCL. Note that nz = 512 and $k = 1 \times 10^5$ unless otherwise stated. (Colour online)

et al. (2019), Agasthya et al. (2025) and Oishi and Brown (2024) where the fixed upper temperature condition prevents this adjustment.

3.1. Parameter sensitivity of the basic state conditional instability

In this section, we analyse the sensitivity of the conditional instability of basic state environments to the climate parameters, by analysing buoyancy profiles and several diagnostics. We first illustrate the parameter dependence of the conditional instability by computing buoyancy profiles of both the basic state and a lifted surface parcel for different parameter values in figure 5.

The top left panel of figure 5 shows how the surface temperature affects the conditional instability in the basic state environment. By comparing the (cooler) blue and (warmer) red profiles, we find that increasing the surface temperature (by ~ 10 K, as in Wing et al. 2018) causes the LFC to increase, the CIN to increase and the pCAPE to decrease. We find that the changes in the conditional instability associated with increasing the surface temperature behave monotonically, at least for the range of parameters considered in our study. The reduction in conditional instability with increasing surface temperature is due to the increased curvature of both the parcel and basic state buoyancy profiles, as a result of the presence of more moisture in the system associated with warmer surface temperatures.

The effect of surface relative humidity on the conditional instability is shown in the top right panel of figure 5. We find that changing the surface relative humidity from 20% to 99% causes a significant decrease in the LFC and CIN, relative to the small increase in pCAPE. Note that in the limit $RH_{surf} \rightarrow 0$, the LFC $\rightarrow 0$ if the environment is dry unstable (as it would be for the basic state with dry adiabatic BCs at the top boundary), indicating that the dependence of the conditional instability (LFC, CIN and pCAPE) on the surface relative humidity does not behave monotonically.

The effect of increasing the radiative cooling and Rayleigh number on the conditional instability is illustrated by the bottom panels of figure 5. Since the (dashed) parcel profile is independent of both r & Ra, changes in conditional stability are due to changes in the

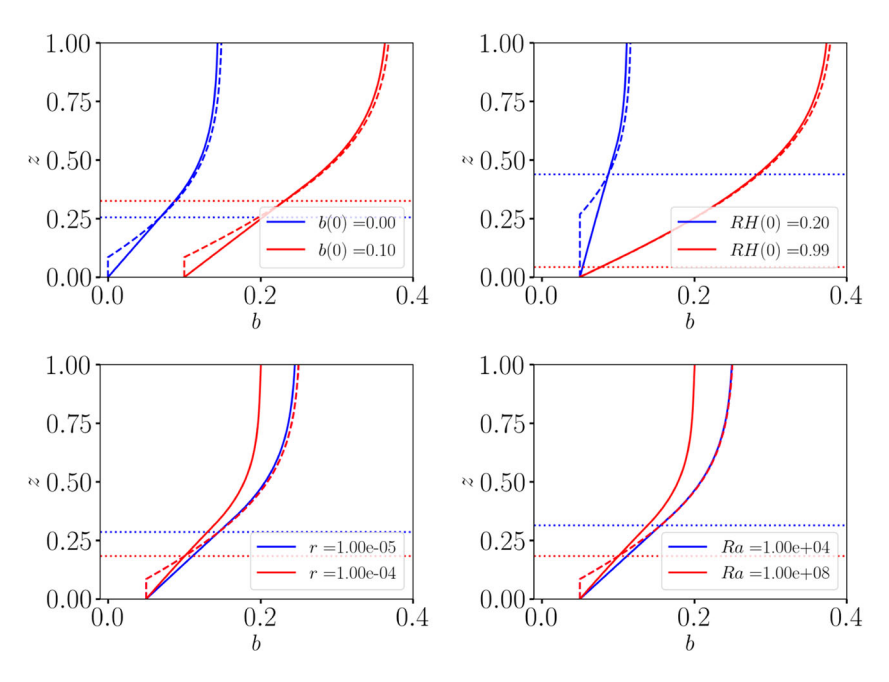


Figure 5. Parcel (dashed) and basic state (solid) profiles for varying: surface temperature (top left), surface relative humidity (top right), radiative cooling rate (bottom left) and Rayleigh number (bottom right). Unless otherwise stated (in the plot legend), the set of parameter values used are $b_{\rm surf} = 0.05$, $RH_{\rm surf} = 0.6$, $r = 10^{-5}$ & $Ra = 10^{6}$. (Colour online)

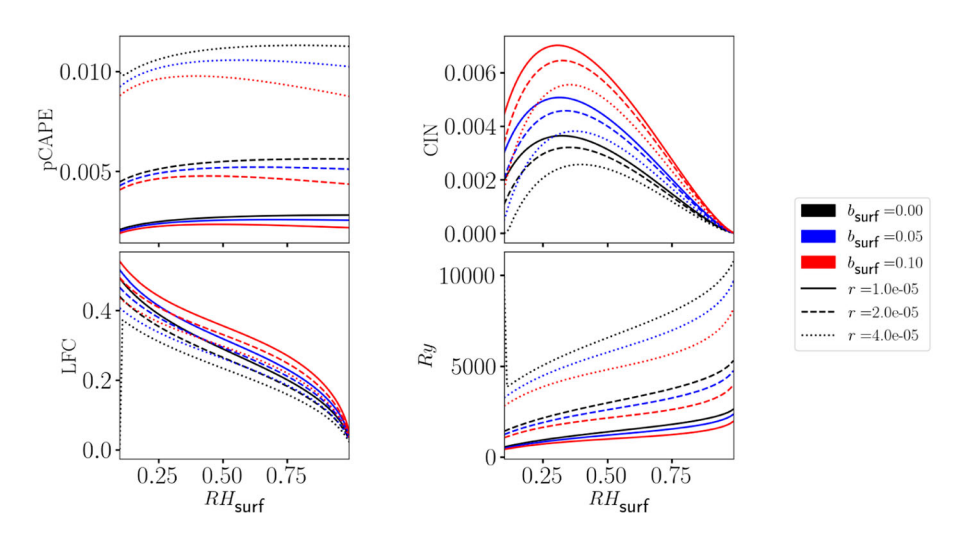


Figure 6. Conditional instability diagnostics (for the basic state) as a function of the surface relative humidity. The different line colours represent different values of surface temperature increase, and the different line styles represent different radiative cooling rates. The Rayleigh number is held fixed at $Ra = 10^6$. (Colour online)



basic state solution. Increases in r and Ra have the same (monotonic) effect on conditional instability: they both cause a decrease in the LFC, increase in the CIN and a significant increase in the pCAPE, relative to the changes in pCAPE caused by changing b_{surf} or RH_{surf} .

3.1.1. Conditional instability and moisture diagnostics

To examine how the basic state changes under climate change (increasing both $r \& b_{surf}$), we can compute both conditional instability diagnostics (pCAPE, CIN, LFC & Ry), and moist diagnostics (P,z_s) . We consider the effects of the typical climate change scenario, and alternative climate change scenarios, on the system, by computing conditional instability and moisture diagnostics with the surface relative humidity, for a fixed set of surface temperatures and radiative cooling values, and additionally fixed $Ra = 10^6$. We plot the diagnostics against surface relative humidity since the conditional instability diagnostics have a non-monotonic relationship with RH_{surf} , but vary monotonically with b_{surf} , r & Ra.

The analysis in section 2.6 showed that the Rainy number is a useful parameter to understand the behaviour of the basic state environment: if $Ry = pCAPE \times (1 - LFC)^2 \times Ra$ increases, we expect increased levels of (moist conditional) instability in our system. The Rainy number is shown in the bottom right panel of figure 6. In general we see that Ry increases with RH_{surf} (for fixed r and b_{surf}). For varying RH_{surf} , changes in Ry are dominated by changes in the LFC rather than changes in pCAPE. The kink in Ry along the black dotted line (as $RH_{surf} \rightarrow 0$) indicates the transition from a moist conditionally unstable atmosphere (where LFC, CIN > 0), to a (dry) absolutely unstable atmosphere $(b_p \ge b_E \ \forall z \in [0,1] \implies \text{LFC}, \text{CIN} = 0)$. We find that increasing b_{surf} (with RH_{surf} and rfixed) causes Ry to decrease, as a result of both the LFC increasing and the pCAPE decreasing. Similarly, Ry increases with r (assuming b_{surf} and RH_{surf} remain fixed), as a result of both the LFC decreasing and the pCAPE increasing with increasing radiative cooling. Figure 7 shows how the moisture in the basic state changes under climate change, characterised by precipitation term (P, defined in section 2.4) and the LCL (z_s) of the basic state: *P* increases in response to increases in all of the climate parameters $(r, b_{surf} \& RH_{surf})$, however z_s decreases with increasing r and RH_{surf} , but increases with increasing b_{surf} . Considering both figures 6 & 7 together, it follows that the r is the most important parameter (for fixed Ra) in affecting the degree of stability in the model (characterised by Ry), however b_{surf} and RH_{surf} are key parameters for affecting the amount of moisture is in the system, since changes in r does not affect the value of P or z_s nearly as much as changes in RH_{surf} or b_{surf} .

The response of the moist instability in the system to different climate change scenarios can be considered by examining the response of Ry to an increase in both the radiative cooling rate and the surface temperature, together. Recall that the typical climate change scenario involves increasing both r from 1×10^{-5} to 2×10^{-5} and b_{surf} from 0.0 to 0.1, assuming that RH_{surf} remains constant. In figures 6 and 7, the typical climate change scenario therefore involves going from the black solid line to the red dashed line, keeping the surface relative humidity fixed. Under the typical climate change scenario, figure 6 shows that Ry increases, and figure 7 shows P and z_s also increase (for the basic state). Both P and z_s increase indicating that climate change causes increased levels of moist instability (in the basic state). Under the typical climate change scenario, the increased moist instability is dominated by effect of r on Ry, whereas the increased levels of moisture are primarily associated with the effect of b_{surf} on P. The basic state analysis therefore indicates that

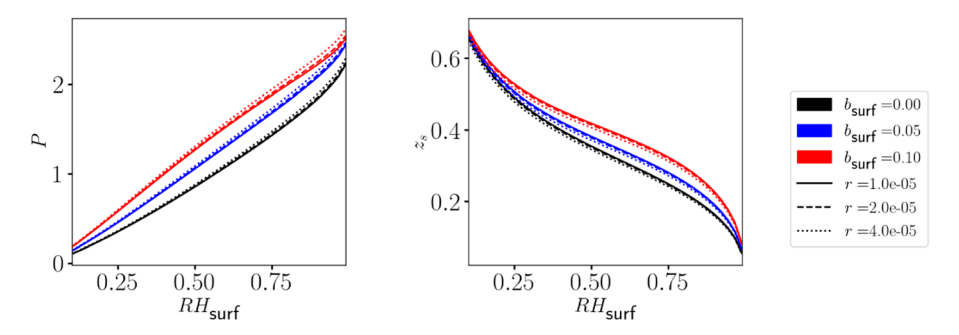


Figure 7. Basic state moisture diagnostics (precipitation, P, and the LCL, z_s) as a function of the surface relative humidity. The different line colours represent different values of surface temperature increase, and the different line styles represent different radiative cooling rates. The Rayleigh number is held fixed at $Ra = 10^6$. (Colour online)

there will be more intense moist convection under climate change, due to increased moist instability and precipitation (over a smaller vertical region) in the basic state environment.

4. Linear stability analysis

Analysis of linear stability can been used to provide initial insight into numerical (non-linear) simulations. In the textbook Chandrasekhar (1961), linear stability is analysed for dry classical Rayleigh-Bénard convection, to find the critical Rayleigh number and the corresponding wavenumber. For Rayleigh numbers greater than the critical Rayleigh number, convection sets in. Vallis *et al.* (2019) found that for Rayleigh numbers that are just slightly greater than critical Rayleigh number, a series of steady convective updraughts are produced in the non-linear simulations. For dry Rayleigh-Bénard convection, as the Rayleigh number is increased the regime of convection shifts from conductive ($Ra < Ra_c$) to steady (for $Ra > Ra_c$), to periodic, before becoming turbulent (see Waleffe *et al.* 2015). Finding the critical Rayleigh number (which varies with the parameters) allows one to compare non-linear simulations for different parameter values by running these simulations at the same supercriticality (e.g. $5 \times Ra_c$). The critical wavenumber also provides an initial indication of how the width of the plumes may respond to change in the parameters. Therefore, we perform a linear stability analysis for the Rainy-Bénard model here.

We set up the eigenvalue problem by perturbing the basic state, $q=\bar{q}+q'$, and assuming the linear wave ansatz, $q'=\hat{q}(z)e^{i(k_xx+k_yy-\sigma t)}$. The model equations can be reduced to the eigenvalue problem,

$$-i\sigma\,\hat{u} = -ik_x\hat{\phi} + \frac{1}{Ra^{1/2}} \left(\frac{\mathrm{d}^2}{\mathrm{d}z^2} - k^2\right)\hat{u},\tag{36}$$

$$-i\sigma\hat{v} = -ik_y\hat{\phi} + \frac{1}{Ra^{1/2}} \left(\frac{\mathrm{d}^2}{\mathrm{d}z^2} - k^2\right)\hat{v},\tag{37}$$

$$-i\sigma\,\hat{w} = -\frac{\mathrm{d}\hat{\phi}}{\mathrm{d}z} + \hat{m} - \gamma\,\hat{q} + \frac{1}{Ra^{1/2}} \left(\frac{\mathrm{d}^2}{\mathrm{d}z^2} - k^2\right)\hat{w},\tag{38}$$

$$-i\sigma\,\hat{m} = -\hat{w}\frac{\mathrm{d}\bar{m}}{\mathrm{d}z} + \frac{1}{Ra^{1/2}}\left(\frac{\mathrm{d}^2}{\mathrm{d}z^2} - k^2\right)\hat{m},\tag{39}$$

$$-i\sigma \hat{q} = -\hat{w}\frac{\mathrm{d}\bar{q}}{\mathrm{d}z} - \frac{(1+\alpha\gamma\,\bar{q}_s)\hat{q} - \alpha\bar{q}_s\hat{m}}{\tau} \left\{ \mathcal{H}(\bar{q}-\bar{q}_s) + (\bar{q}-\bar{q}_s)\,\mathrm{d}\mathcal{H}(\bar{q}-\bar{q}_s) \right\} + \frac{1}{Ra^{1/2}} \left(\frac{\mathrm{d}^2}{\mathrm{d}z^2} - k^2 \right) \hat{q}, \tag{40}$$

$$-\frac{\mathrm{d}\hat{w}}{\mathrm{d}z} = ik_x\hat{u} + ik_y\hat{v},\tag{41}$$

with boundary conditions

$$\hat{m}(0) = 0, \quad \hat{q}(0) = 0, \quad \hat{\mathbf{u}}(0) = \mathbf{0},$$
 (42)

$$\frac{\hat{dm}}{dz}(1) = 0, \quad \left\{ 1 + \alpha \gamma \, \bar{q}_s(1) \right\} \hat{q}(1) - \alpha \bar{q}_s(1) \hat{m}(1) = 0, \quad \hat{\mathbf{u}}(1) = \mathbf{0}. \tag{43}$$

Note that $k^2 \equiv k_x^2 + k_y^2$, and, a first order Taylor expansion is used to express $q_s' \approx \alpha \bar{q}_s b'$. In this formulation, we have replaced $b' = m' - \gamma q'$ in order to implement the upper moist pseudoadiabatic boundary conditions. The second boundary condition in equation (43) is equivalent to $q = q_s$. We solve the eigenvalue problem numerically using the Dedalus framework (Burns *et al.* 2020).

The eigenvalue problem given by equations (36)–(43) is for a smooth approximation of the Heaviside function, which allows \mathcal{H} to be Taylor expanded (about $\bar{q} = \bar{q}_s$). We approximate $\mathcal{H}(f) = \frac{1}{2}(1 + \operatorname{erf}(kf))$ with $k = 10^3$ so that, $d\mathcal{H}(f) = \frac{k}{\sqrt{\pi}}e^{-(kf)^2}$. Oishi and Brown (2024) argued that $\bar{q} - \bar{q}_s$ is the same order of magnitude (or smaller) as the perturbations in the vicinity of the LCL, and therefore that terms involving $(\bar{q} - \bar{q}_s)$ d $\mathcal{H}(\bar{q} - \bar{q}_s)$ are nonlinear and should be neglected. This assertion only considers the leading order solution, for which $\bar{q} = \bar{q}_s$ in saturated regions. However for the higher order solution found in section 3, $\bar{q} - \bar{q}_s \sim \mathcal{O}(\epsilon)$ is finite and non-zero in the upper saturated region (as shown by C(z) in figure 3). Therefore the $d\mathcal{H}$ term is also finite and non-zero, and independent of the amplitude of the perturbation considered. Nevertheless, the linear stability results (spectra, eigenvectors, etc.) presented in Oishi and Brown (2024) are broadly similar to those shown in the present study, since the $d\mathcal{H}$ term is relatively small. We argue that including the $d\mathcal{H}$ term is required for a consistent calculation of the onset of convection, when comparing with non-linear simulations which use a smooth approximation of the Heaviside function.

To compute the critical Rayleigh number (Ra_c) , we first calculate the basic state for smooth \mathcal{H} (numerically) for a given Rayleigh number (Ra). The numerical basic state solution is obtained by using Dedalus to solve the non-linear boundary value problem (given by equations (28)–(31), and a smooth Heaviside function), with the $\mathcal{O}(\epsilon)$ accurate analytical solution used as an initial guess (to speed up convergence). We then solve the eigenvalue problem for a range of wavenumbers, $k = \sqrt{k_x^2 + k_y^2}$, and determine k_{max} which maximises the growth rate $(\Im(\sigma))$. We adjust Ra iteratively, and repeat the above method, until the absolute value of the maximum growth rate is less than a tolerance, which we take to be 10^{-8} . The pair (Ra, k_{max}) which satisfies these conditions determines the critical Rayleigh number, Ra_c , and the critical wavenumber, k_c .

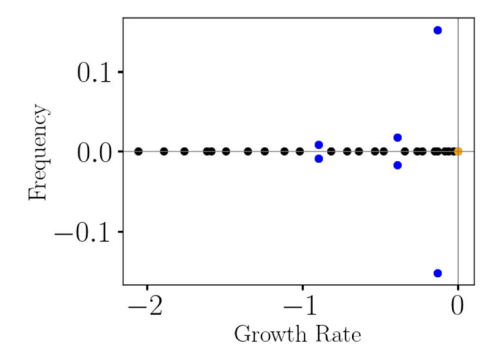


Figure 8. Eigenvalue spectra at criticality $Ra = Ra_c$, $k = k_c$. The blue dots show damped oscillatory modes, and the black dots show purely decaying modes. The results are shown for the parameter values: $RH_{surf} = 0.6$, $b_{surf} = 0.05$ and $r = 1 \times 10^{-5}$ and $Ra = Ra_c = 7.80 \times 10^{5}$. (Colour online)

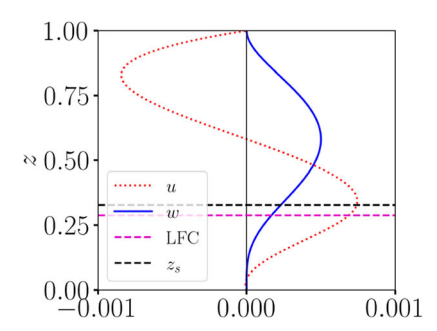
An example of the eigenvalue spectra for an unsaturated atmosphere ($RH_{surf} < 1$) at criticality is shown in figure 8. The maximum growing mode (yellow dot) has zero growth rate and frequency. Note that the damped oscillatory modes are only present for unsaturated cases: in the saturated limit ($RH_{surf} = 1$), there are no decaying oscillatory modes, i.e. all eigenvalues have zero frequency, indicating that the damped waves associated with the decaying oscillatory mode can only exist in the lower unsaturated region of the domain. The waves associated with the damped oscillatory mode are associated with dry gravity waves, and we derive an approximate form for their dispersion relationship in section 4.2.

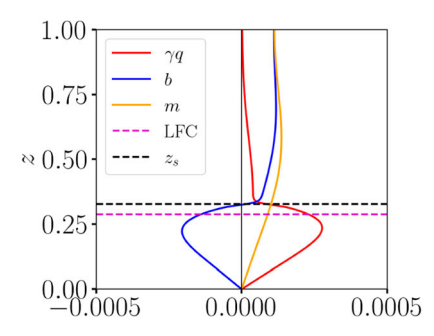
4.1. Action of the linear perturbation

In this section we examine the structure of the eigenvectors, the perturbations and their impact on the basic state, in terms of their effect on moisture and conditional instability. We compute the eigenvectors and perturbations corresponding to the fastest growing mode, at criticality ($Ra = Ra_c \& k = k_c$). Note that we define a (real) perturbation quantity, associated with an eigenvector, as for example $w' = \Re(\hat{w}(z)e^{ikx})$.

Figure 9 shows the vertical structure of the normalised eigenvectors. The eigenvectors are normalised such that $\max(w_r) = 5 \times 10^{-4}$ with $w_i = b_i = q_i = u_r = 0$. The eigenvector represents the perturbation in an updraft region (since $\max(w') > 0$). We can consider the perturbation in a subsiding region (where $\max(w') < 0$), by multiplying the eigenvectors in figure 9 by a factor of -1.

The structure of the b and \hat{q} eigenvectors in figure 9 reveals that the linear perturbation causes a moistening of updraft regions, and makes the updrafts more buoyant (b' > 0 for $z > z_s$). Assuming $x = 0 \Rightarrow w' = \hat{w}$, $b' = \hat{b}$, $q' = \hat{q}$, etc., the relative humidity is given by $RH = q/q_s \approx (\bar{q} + q')/(\bar{q}_s(1 + \alpha b')) \Rightarrow RH' \approx (q' - \alpha \bar{q}b')/\bar{q}_s$. Below z_s , b' < 0 and $q' > 0 \Rightarrow RH' > 0$, so the linear perturbation moistens the updrafts in the lower (unsaturated) region. Computation of the perturbation relative humidity reveals that $RH' \geq 0$ for $z \geq z_s$ too, i.e. $q' \geq \alpha \bar{q}b'$ despite increase in q_s due to warming. However the increase in RH is much larger in the lower unsaturated region than it is in the upper saturated region, as a result of the small condensational timescale causing $q' \approx \alpha \bar{q}_s b'$ (in the saturated region),





where \bar{q}_s is decaying exponentially with height. The moistening effect of the linear perturbation in updraft regions results in increased levels of condensation, and a decrease in z_s in updraft regions. The linear perturbation has the opposite effect in subsiding regions, causing a drying effect which reduces the levels of condensation and increases z_s .

To assess the effect of the linear perturbation on the conditional stability, we examine the structure of the perturbation b'. The parcel buoyancy profile remains the same, however the buoyancy profile of the environment changes with the linear perturbation. The \hat{b} eigenvector in figure 9 shows the effect of the linear perturbation in an updraft region. For $z < z_s$, $b' = \hat{b} < 0$, so that the linear perturbation is making the environment less buoyant. Recalling figure 1, this reduces the CIN in the lower region, and causes the LFC (where $b_p = b_E$) to decrease. There is a small vertical region above the LFC for which b' < 0, and so the pCAPE in the region is increasing. However, above z_s , the linear perturbation makes the environment more buoyant since b' > 0 here, which reduces the pCAPE. Therefore, the linear perturbation acts in updraft regions by making the lower levels more unstable by reducing the CIN, LFC and increasing the pCAPE in a small vertical region just above the LFC, however, it has a stabilising influence on the upper levels, causing a reduction in the overall pCAPE. The effect of the linear perturbation on the subsiding regions is opposite to that in the updraft regions: the linear perturbation acts by stabilising the lower levels up to just above the LFC, and destabilises the upper levels.

The modal structure of the perturbation quantities over one wavelength is exhibited in figure 10. Note that the eigenvectors are normalised with $\max(w_r) = 2 \times 10^{-3}$ to keep the perturbations small, relative to the basic state solution (to be consistent with figure 11). The arrows show the circulation from the moister updraft regions to the drier subsiding regions. The perturbations b' & q' show sharp changes in gradient around the saturation point, z_s (also shown in figure 9). Note for this set of parameter values, in the updraft regions, there is a small region where w' < 0 close to the surface, although the magnitude of w' is small compared to $\max(w')$ in the column. Figure 10 shows that w', b' & q' are all in phase, with

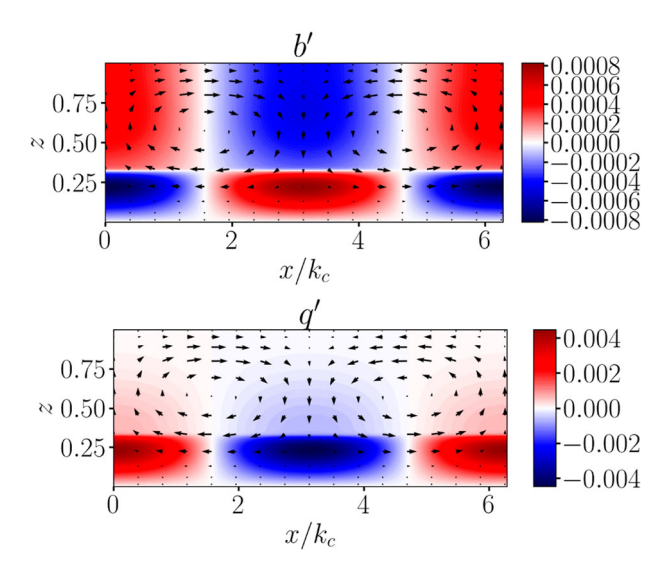


Figure 10. The real parts of the buoyancy and specific humidity perturbation quantities at criticality. The perturbation quantities are calculated using $f'(x,z) = \hat{f}(z)e^{ik_Cx}$, where $\hat{f}(z)$ denotes the eigenvector of the quantity f. The velocity is shown by the black arrows. The results are shown for the parameter values: $RH_{surf} = 0.6$, $b_{surf} = 0.05$ and $r = 1 \times 10^{-5}$ and $Ra = Ra_c = 7.80 \times 10^5$. (Colour online)

the circulation from the moister updraft regions to the drier subsiding regions associated with u' being $\pi/(2k_c)$ out of phase with w' as expected.

Figure 11 shows the condensation field over one wavelength, produced by adding the enlarged linear perturbation (shown in figure 10) to the basic state. We take $b = \bar{b} + b'$, $q = \bar{q} + q'$ and compute $C = \gamma (q - q_s) \mathcal{H}(q - q_s)$, where $q_s = e^{\alpha(b-z)}$. We choose the perturbations to be relatively small for illustration ($b' \ll \bar{b}$), so that the b and q fields do not show visible changes. However the linear perturbation causes a visible change in the condensation field. The panels in figure 11 show two pockets around the LCL, where condensation has been most greatly enhanced by the moistening effect of the linear perturbation in updraft regions.

The results in figures 9, 10 & 11 indicate that the linear perturbation causes instability to occur in the updraft regions around the LCL, by consuming pCAPE in the upper regions $(z \ge z_s)$, moistening the overall column and reducing the lower level inhibition by reducing the CIN and the LFC. It further increases pCAPE in a small vertical region between the LFC and the LCL. The moistening causes the largest increase in condensation around the LCL of the environment, indicating that the instability stems from this region of the domain.

4.2. Approximate dispersion relationship for highest frequency modes

The eigenvalue spectra shown in figure 8 revealed the presence of damped oscillatory modes. Oishi and Brown (2024) assumed that the oscillatory modes are dry Boussinesq internal gravity waves, and examined the associated eigenvector structure of the modes to obtain an estimate for the moisture modified internal gravity waves. We also assume the waves are dry internal gravity waves, but use a different vertical wavenumber estimate motivated by the structure of the b and q eigenvectors.

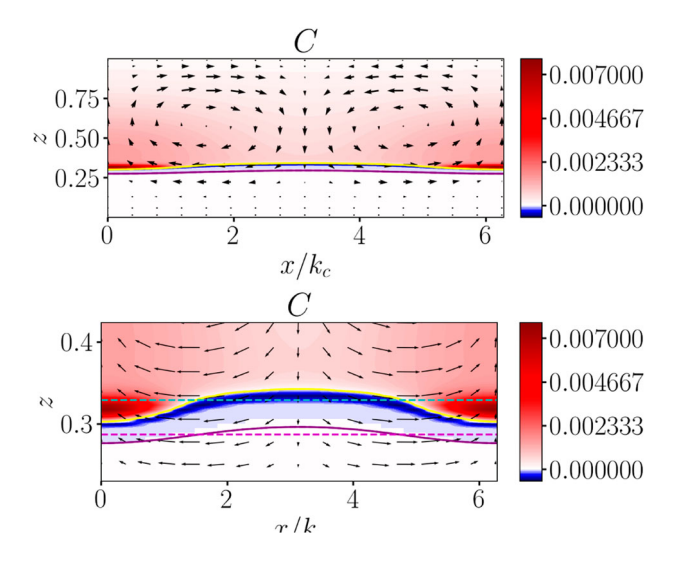


Figure 11. condensation field $C = \gamma (q - q_s) \mathcal{H}(q - q_s) / \tau$, shown over one horizontal wavelength. The top panel shows C for the full vertical domain, and the bottom panel shows a zoom of C around the LCL of the environment, where the impact of the linear instability on the basic state is most pronounced. The cyan and magenta line mark the LCL and LFC of the environment respectively (with the dashed lines marking the basic state values). The black arrows show the velocity (u, w). The results are shown for the parameter values: $RH_{\rm surf} = 0.6$, $b_{\rm surf} = 0.05$ and $r = 1 \times 10^{-5}$ and $Ra = Ra_c = 7.80 \times 10^5$. (Colour online)

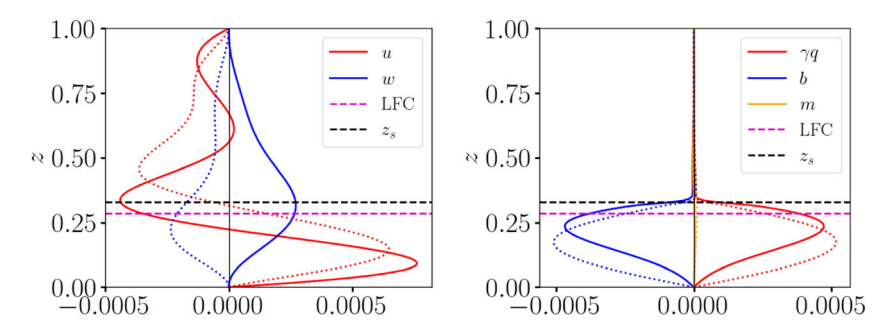


Figure 12. An example of the normalised eigenvectors at criticality, $Ra = Ra_c \& k = k_c$, associated with the highest frequency mode. Note that the solid and dotted lines represent the real and imaginary parts of the eigenvectors, respectively. The left panel shows the u and w eigenvectors, whilst the right panel shows the b, γq and m eigenvectors. The dashed lines mark the basic state LCL (z_s , red) and the LFC (blue). The results are shown for the parameter values: $RH_{surf} = 0.6$, $b_{surf} = 0.05$ and $r = 1 \times 10^{-5}$ and $Ra = Ra_c = 7.80 \times 10^5$. (Colour online)

The highest frequency normalised eigenvectors are shown in figure 12. The buoyancy and humidity eigenvectors are trapped below the LCL, in the unsaturated region of the domain. The imaginary part shown by the dotted lines corresponds to a tilt of the modal structure.

Recall that the dispersion relationship for Boussinesq internal gravity waves is given by,

$$\omega_r = \frac{N_b k_x}{\sqrt{k_x^2 + k_z^2}}.$$

We obtain an approximate dispersion relationship for ω_r by estimating N_b and k_z . We estimate the Brunt–Väisälä frequency by $N_b=\partial b/\partial z(z=0)$, where b is the full buoyancy field. In Oishi and Brown (2024), the vertical wavenumber was specified by the full domain height $(L_z=1)$, i.e. $k_z=2\pi/L_z$. However, the structure of the b & q eigenvectors exhibit one peak (half of a wave) confined to the unsaturated region $(0 \le z \le z_s)$, which motivates the choice of a vertical wavenumber of $k_z=\pi/z_s$ for the moist system. We write the approximate dispersion relationship for the moisture modified internal gravity waves as,

$$\omega_r \approx \frac{\partial b/\partial z|_{z=0} k_c}{\sqrt{k_c^2 + (\pi/z_s)^2}} \tag{44}$$

Note that, in the non-linear system, internal gravity waves cause triggering of convection and are themselves generated by convective plumes (Vallis *et al.* 2019). We examine the approximate relationship across the parameter space in the following section.

4.3. Parameter dependence of the linear perturbation

To investigate how the values of the climate parameters change the action of the linear perturbation (at criticality) on the system, we examine changes in the critical parameters, the action on conditional instability, and in the structure of the buoyancy and moisture fluxes, as parameters are varied.

We first look at how the values of the critical Rayleigh number, Rainy number and wavenumber change with the parameters. Figure 13 shows Ra_c , Ry_c , k_c and $\max(\omega_r)$ as a function of the surface relative humidity, for various different surface temperature increases and radiative cooling rates. Recall that the value of Ra only reflects the value of diffusion in our system; it cannot change according to changes in moist stability, and so it fundamentally fails to capture the moist convective behaviour. The critical Rainy number varies much less than the Rayleigh number across the climate parameter space, as a consequence of the incorporating a quantification of moist stability in its definition: Ra_c varies by a factor of ~ 8.0 across all of the parameter values, whereas Ry_c varies by a factor of ~ 2.1 . The Rainy number captures the ratio of conditional instability (quantified by pCAPE and its associated length scale) to diffusion, and it therefore follows that the Rainy number is the more useful parameter for describing the state of the moist system.

Recall figure 2, which also shows the critical dry Rayleigh and critical Rainy numbers (in the first column), but across the surface temperature – radiative cooling parameter space. We consider larger radiative cooling rates in figure 2 than in figure 13 to get a better picture of the sensitivity to the radiative cooling rate. The critical Rayleigh numbers found in Vallis *et al.* (2019) and Oishi and Brown (2024) are smaller than those found here, due to a combination of factors: our temperature scale is two times larger than theirs, we have flux psuedoadiabatic upper boundary conditions unlike their fixed boundary conditions, and we additionally have a radiative cooling term. The results in figure 2 show that the critical dry Rayleigh number is more sensitive to the radiative cooling rate than the surface temperature, indicating that the cooling rate is primarily responsible for driving the

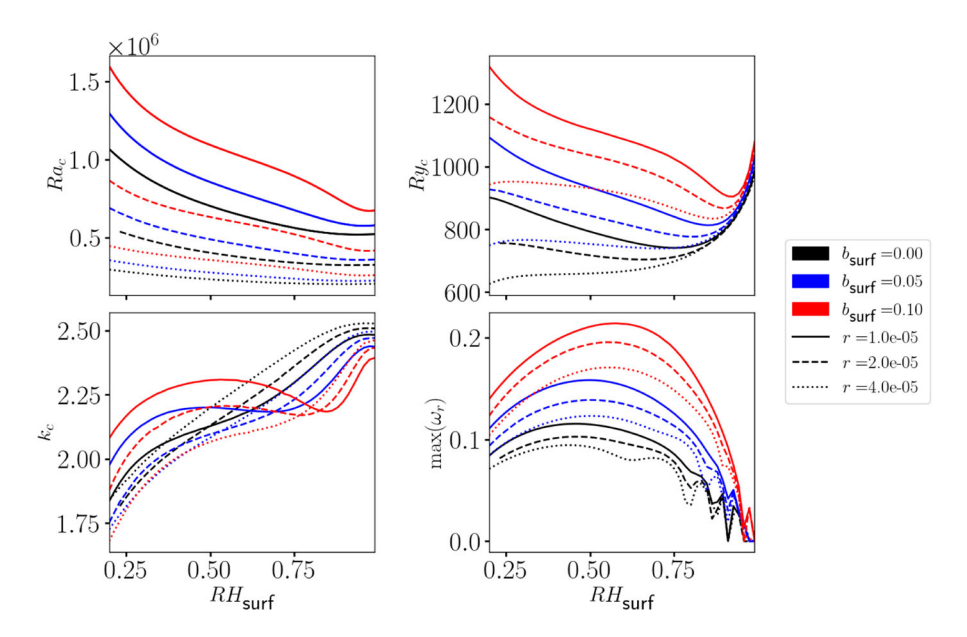


Figure 13. Critical Rayleigh (top left), Rainy (top right) and wavenumber (bottom left), and the highest frequency (bottom right) as functions of the surface relative humidity. The different line colours represent different surface temperature increases, and the different line styles represent different radiative cooling rates. The idealised climate change scenario involves going from the black solid line to the red dashed line, keeping the surface relative humidity fixed. (Colour online)

instability in the system. The reason for the variation can be seen by recalling the buoyancy profiles in figure 5: the profiles are shown for the end values across the parameter space, and we can see that the increase in CAPE associated with increasing the radiative cooling rate (from $r=1\times 10^{-5}$ to $r=1\times 10^{-4}$) is far greater than the decrease in CAPE and increase in CIN associated with increasing the surface temperature (from $b_{\text{surf}}=0$ to $b_{\text{surf}}=0.1$). Again, the results of figure 2 show that the critical Rainy number varies much less than the critical Rayleigh number across this cut of the surface temperature – radiative cooling parameter space.

For the typical idealised climate change scenario (comparing the black solid line to the dashed red line, for fixed RH_{surf}) we see an increase in Ry_c in figure 13. The critical Rainy number increases as a result of increased moisture levels (associated with warmer surface temperatures): both the parcel and (basic state) environment profiles become warmer, increasing curvature of the moist pseudoadiabat, and result in an increase in CIN (and the LFC – see figure 5). With increased levels of inhibition, pCAPE must be higher for the system to become unstable, and so Ry_c increases under climate change. The increased levels of inhibition and the higher levels of available potential energy point to an intensified water cycle, characterised by stronger ($w^2/2 \sim \text{pCAPE}$) more intermittent (higher CIN) convection. It is worth noting that Ry_c is independent of b_{surf} and r in the saturated limit, however Ra_c varies significantly, indicating that pCAPE $\sim 1/Ra_c$ as $RH_{\text{surf}} \rightarrow 1$ (since the LFC \rightarrow 0).

The critical wavenumber provides information about the width of the linear modes (i.e. updraft and subsiding regions). Note that the width of the updraft and subsiding regions are

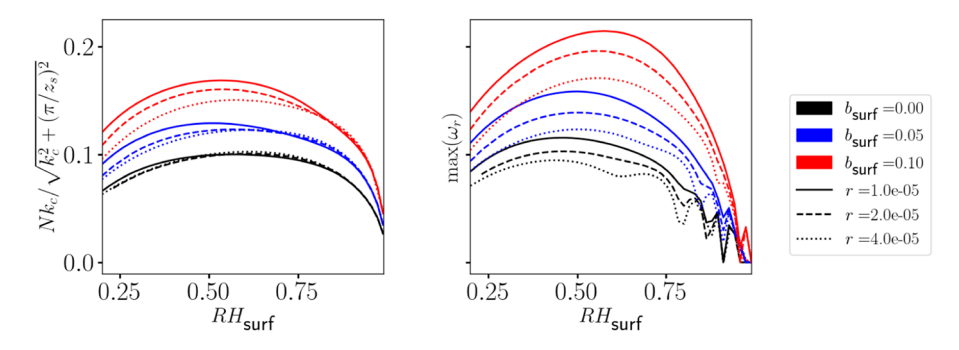


Figure 14. Dispersion relationship for the highest frequency mode (left), and the highest frequency mode calculated by solving the eigenvalue problem (right). The curves are all calculated at criticality ($Ra = Ra_c$). The different line colours represent different surface temperature increases, and the different line styles represent different radiative cooling rates. The idealised climate change scenario involves going from the black solid line to the red dashed line, keeping the surface relative humidity fixed. (Colour online)

necessarily equal in the linear analysis, however this is not typically observed in non-linear simulations (Agasthya *et al.* 2025). The linear theory does provide an initial indication of how we may expect convective plume widths to scale with the climate parameters. Examining the bottom left panel of figure 13, we see that under the climate change scenario, if $RH_{surf} > 0.6$, k_c decreases and the updraft and subsiding regions get wider. However, if $RH_{surf} < 0.6$, we see the opposite effect, with the updraft and subsiding regions becoming narrower.

Recall that the waves associated with the damped maximum frequency mode are damped (linear) dry internal gravity waves. The bottom right panel of figure 13 shows the (maximum) frequency associated with the dry internal gravity waves, as a function of the parameters. We see that under a typical climate change scenario (going from black solid to red dashed line, with RH_{surf} fixed), the maximum frequency increases, which is associated with an increase in the triggering of convection. However, the triggering is reduced by increased CIN levels in the lower unsaturated region of the domain under climate change. In section 4.2, we derived an estimate for the frequency of these moisture modified internal gravity waves. That approximate dispersion relationship is shown against the calculated maximum frequency values in figure 14. We see a qualitative agreement between the approximate and actual values of the maximum frequency. The approximate maximum frequency does tend towards zero in the saturated limit, and also captures the decrease in frequency as $RH_{surf} \rightarrow 0.20$. There are discrepancies in the position and magnitude of the peak between the approximate and actual values of the maximum frequency. Note that the dispersion relationship is the best fit for the lines with $b_{surf} = 0$, in which domain moisture is at a minimum (relative to the other curves). The moisture modified internal gravity waves are responsible for triggering convection in the non-linear system (Vallis et al. 2019), and so understanding how their frequency changes under climate change gives us some initial insight into how we may expect the non-linear behaviour to respond.

We could regard the (most unstable) linear mode as large scale on a global domain, and consider how it would effect the conditional instability of embedded storms. The effect of the linear perturbation on the conditional instability is shown by looking at the structure

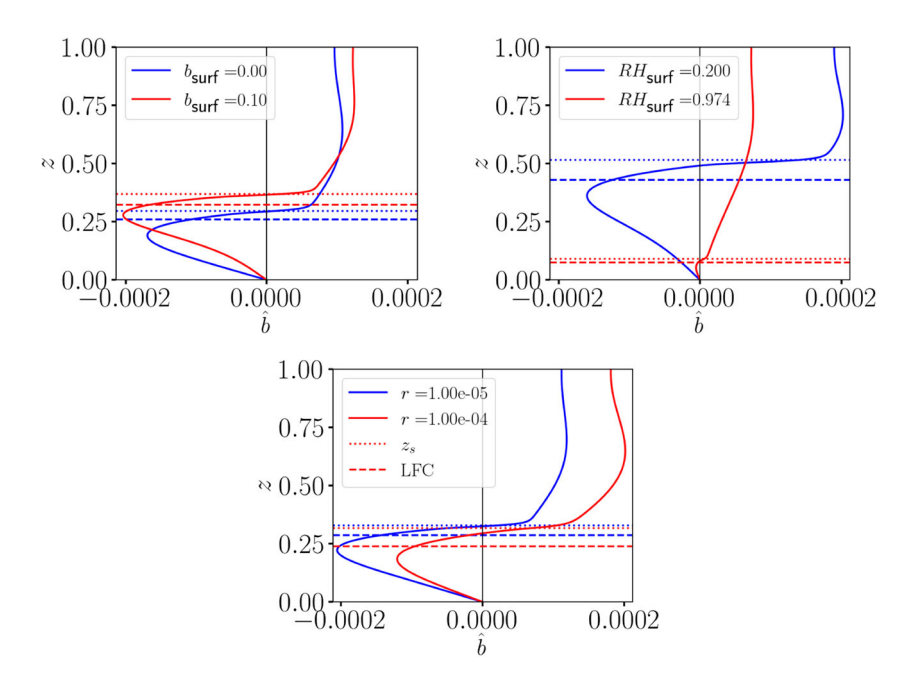


Figure 15. Buoyancy eigenvectors at criticality, plotted for varying: surface temperature (top left), surface relative humidity (top right), and radiative cooling (bottom). Dashed lines mark the LFCs and dotted lines mark the LCLs of the different environments. The eigenvectors are normalised such that $\max(w_r) = 5 \times 10^{-4}$ and $w_i = 0$. (Colour online)

of the buoyancy eigenvectors in figure 15. Since the parcel profile is not influenced by \hat{b} , the vertical regions where $\hat{b} < 0$ cool the environment and result in a reduction of inhibition (if $b_p < b_E$) or increase in instability (if $b_p > b_E$) in the region. Similarly, the vertical regions where $\hat{b} > 0$ cause the environment to warm, which causes an increase in inhibition or a decrease in instability in that region. The buoyancy eigenvectors shown in figure 15 represent the linear perturbation updraft regions. The action of the linear perturbation in an updraft region on the conditional instability remains the same, for each of the different parameter values: $\hat{b} < 0$ in the lower region, which extends to just below z_s (and just above the LFC). There is a reduction in the pCAPE in the upper region where $\hat{b} > 0$, and a sharp change in the gradient of \hat{b} (and \hat{q}) just above z_s .

The buoyancy and moisture fluxes can be used to give an initial indication of the non-linear transport of buoyancy and moisture. Figure 16 shows how the horizontally averaged vertical transport of the buoyancy perturbation ($\hat{w}\hat{b} \sim \langle w'b' \rangle$) changes with the climate parameters. Apart from the $RH_{\text{surf}} = 0.974$ case, all of the buoyancy fluxes w'b' display a similar structure: they have a negative peak of flux in the lower region, which occurs just below the LFC and a larger positive peak in the upper region. The height of the positive peak is dependent on z_s , such that if z_s increases, we expect the height of the positive flux to increase with it. The nearly saturated $RH_{\text{surf}} = 0.974$ case does not exhibit a significant region of negative flux, which we conjecture is a result of the CIN being close to zero in this region. The perturbation moisture flux is shown in figure 17. Again, the nearly saturated case shows different behaviour than the rest of the parameter values displayed. The general

behaviour of the moisture flux shows the peak moisture flux occurs around the LFC and below z_s , with a second smaller peak occurring in the upper saturated region. The $b_{surf} = 0.1$ & $RH_{surf} = 0.2$ cases show a small region close to the surface where the moisture flux towards the surface, which is caused by w' < 0 in this region due to the higher levels of CIN in these two cases. Note that the linear perturbation for the nearly saturated $RH_{surf} = 0.974$ case shows a different behaviour to the other cases, with the peaks in the moisture and buoyancy fluxes no longer occurring around the LFC, but around the middle of the domain. Examining the Ry_c panel of figure 13, we see that the critical Rainy number is almost independent of the surface temperature and radiative cooling rate for the nearly saturated regimes, which is a result of low levels of CIN and the LCL causing a different action of the linear perturbation.

5. Discussion

We have presented a detailed analysis of a simple framework for studying changes in moist convection under climate change. The Rainy-Beńard model is set up for climate forcing simulations, by adding a constant radiative cooling term to the buoyancy equation, and choosing appropriate boundary conditions: at the bottom boundary we impose the relative humidity and surface temperature, and at the top boundary we impose moist pseudoadiabatic boundary conditions which give the temperature, buoyancy and humidity at the top boundary freedom to adjust. We also impose idealised no-slip boundary conditions at both boundaries. Climate change can be imposed by careful choice of the climate parameters, namely the surface temperature, the radiative cooling rate and the surface relative humidity: we illustrate a typical climate change scenario by doubling the radiative cooling in response to a 10K increase in surface temperature, keeping the surface relative humidity fixed.

The fundamental linear behaviour of the Rainy-Bénard model has been studied using a basic state analysis (section 3) and a linear stability analysis (section 4), and quantified using both moisture and conditional instability diagnostics. The pseudoadiabtic boundary conditions taken at the top boundary allow realistic adjustment in the basic state solution to close to the neutral parcel profile (figure 4), which is a well-observed feature of tropical convective environments (e.g. Betts 1986) and was not possible in the previous studies by Vallis *et al.* (2019), Agasthya *et al.* (2025), and Oishi and Brown (2024). The basic state analysis reveals that the radiative cooling parameter is primarily responsible for changes in the (basic state) conditional instability, whereas the surface temperature and surface relative humidity are responsible for changes in the (basic state) precipitation (figures 5 and 6).

We used a linear instability analysis to calculate the critical Rayleigh number for convective onset for a range of climate change parameter values, examining the action of the most unstable mode (section 4.1) and the waves associated with the highest frequency mode. The most unstable mode has a moistening action on the updraft (w' > 0) regions of the domain, and a drying action on the subsiding regions (w' < 0) of the domain, with a circulation from the moister updraft regions to the drier subsiding regions (figures 8, 9 and 10). The moisture perturbation is much weaker above the LCL then below, as a result of the condensational timescale being small, which means that $q' \approx \alpha \bar{q}_s b'$ where \bar{q}_s drops off exponentially with height; no such constraint exists on the perturbation in the lower

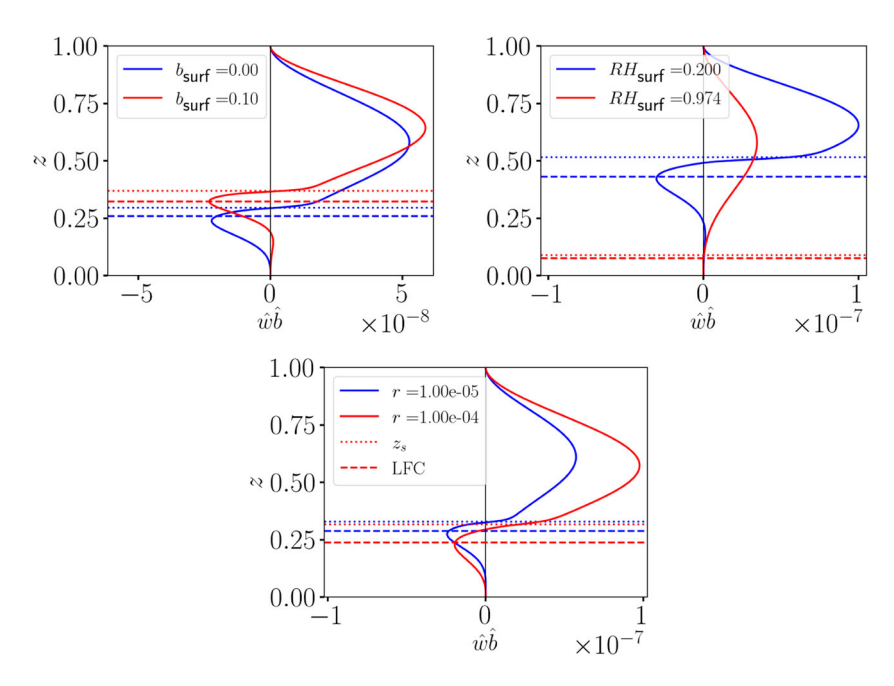


Figure 16. Buoyancy flux w'b' at criticality, plotted for varying: surface temperature (top left), surface relative humidity (top right), and radiative cooling (bottom). Dashed lines mark the LFCs and dotted lines mark the LCLs of the different environments. The eigenvectors are normalised such that $\max(w_r) = 5 \times 10^{-4}$ and $w_i = 0$. (Colour online)

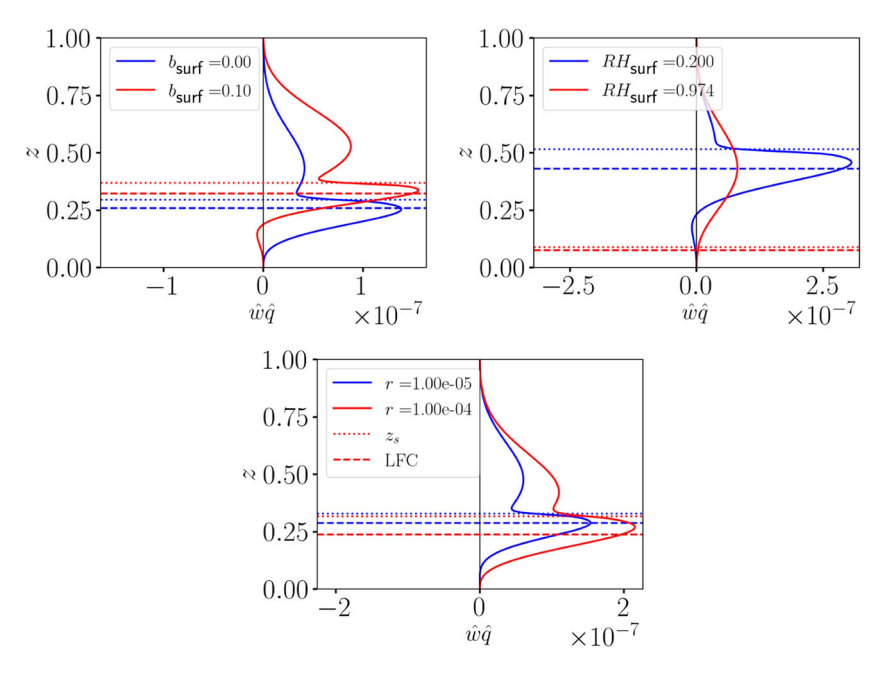


Figure 17. Specific humidity flux w'q' at criticality, plotted for varying: surface temperature (top left), surface relative humidity (top right), and radiative cooling (bottom). Dashed lines mark the LFCs and dotted lines mark the LCLs of the different environments. The eigenvectors are normalised such that $\max(w_t) = 5 \times 10^{-4}$ and $w_i = 0$. (Colour online)

unsaturated part of the domain. In terms of conditional instability, we find that the most unstable mode causes a reduction of both the convective inhibition (CIN) below the LFC, and the pCAPE above the LFC, in the updraft regions. We find damped oscillatory modes associated with dry internal gravity waves trapped in the lower unsaturated region of the domain, as in Oishi and Brown (2024). We derived an approximate dispersion relationship for the dry internal gravity waves in equation (43), which differs from that given in Oishi and Brown 2025, but shows qualitative agreement with the numerically calculated results (figure 13).

A key result is the derivation of non-dimensional parameters which correctly capture the relationship between moist instability and diffusion (section 2.6 and Appendix C). We used the positive convective available potential energy (pCAPE) as a scale for the kinetic energy in the system, and its associated length scale (the difference between the level of neutral buoyancy (LNB) and the level of free convection (LFC)) to construct a moist Rayleigh number, called the Rainy number:

$$Ry = \frac{\text{pCAPE} \times (\text{LNB} - \text{LFC})^2}{\nu \kappa}$$

The Rainy number represents the ratio of (moist) conditional instability (quantified by pCAPE) to diffusion. We find that Ry changes in response to changes in moist instability; Ra does not (figures 1 and 12). By using conditional instability (quantified by pCAPE) to set the scales in the system, the Rainy number is a better control parameter for our model: across the climate parameter space, Ry varies less at criticality than Ra.

Due to the relationship between radiative cooling and pCAPE in our solutions, we are also able to define a radiatively-based Rainy number (see Appendix C). The Radiative Rainy number, which uses a different measure of moist conditional instability, also varies less than Ra at criticality as a result. In fact the use of the CAPE-based or radiatively-based Rainy number is probably an open choice according to the scientific question at hand. CAPEbased Ry would naturally be appropriate for studies of convection and the water cycle; radiatively-based Ry would be a natural control for the system when studying sensitivity to boundary fluxes and radiative forcing.

Under the typical climate change scenario, the basic state analysis results indicate that we expect more intense moist convection, with more rainfall. There is more moisture in the system (associated with warmer surface temperatures) and this leads to a mid-domain profile which is warmer, following a profile which is more "bowed" (figure 5), so despite the warmer and humid surface air, the warmer mid-levels lead to increased CIN under climate change. For the onset of convection to occur in a system with more CIN, the available potential energy (pCAPE) must increase, and as a result the critical Rainy number increases. The increase in the critical Rainy number is associated with an intensification of the water cycle (as found in Kendon et al. 2019): we expect more intense (increased pCAPE $\sim w^2/2$), more intermittent (increased CIN) moist convection under climate change. Our future research will build on this framework and examine non-linear simulations and transport of moist Rainy-Bénard convection under climate change.



Note

1. An alternative definition of conditional instability from the American Meteorological Society Glossary: "The state of a layer of unsaturated air when its lapse rate of temperature is less than the dry-adiabatic lapse rate but greater than the moist-adiabatic lapse rate". For saturated upper profiles, the two definitions of conditional instability are equivalent, but not generally (American Meteorological Society 2023)

Acknowledgments

The authors would like to thank Kasia Nowakowska, Geoff Vallis, Jeff Oishi, Ben Brown, Lokahith Agasthya and David Dritschel for helpful discussions on Rainy-Bénard convection. We would also like to thank Jun-Ichi Yano for his thorough review of this paper, which has lead to its considerable improvement. This work was undertaken on ARC4, part of the High Performance Computing facilities at the University of Leeds, UK.

Disclosure statement

No potential conflict of interest was reported by the author(s).

Funding

This work was supported by the Leeds-York-Hull Natural Environment Research Council (NERC) Doctoral Training Partnership (DTP) Panorama under grant NE/S007458/ and UK Met Office CASE project funding.

ORCID

G. N. Dritschel http://orcid.org/0009-0000-9563-3801 S. M. Tobias http://orcid.org/0000-0003-0205-7716

References

Agasthya, L., Muller, C. and Cheve, M., Moist convective scaling: insights from an idealised model. Quart. J. R. Meteorolog. Soc. 2025, 151, e4902.

American Meteorological Society, Conditional instability, 2023. Available online at: https://glossary. ametsoc.org/wiki/Conditional_instability (accessed 17 December 2024).

Arakawa, A. and Schubert, W.H., Interaction of a cumulus cloud ensemble with the large-Scale environment, part I. J. Atmos. Sci. 1974, 31, 674-701.

Betts, A.K., A new convective adjustment scheme. Part I: observational and theoretical basis. Quart. *J. R. Meteorolog. Soc.* 1986, **112**, 677–691.

Bretherton, C.S., A theory for nonprecipitating moist convection between two parallel plates. Part I: thermodynamics and "Linear" solutions. J. Atmos. Sci. 1987, 44, 1809-1827.

Bretherton, C.S., A theory for nonprecipitating convection between two parallel plates. part II: nonlinear theory and cloud field organization. J. Atmos. Sci. 1988, 45, 2391–2415.

Burns, K.J., Vasil, G.M., Oishi, J.S., Lecoanet, D. and Brown, B.P., Dedalus: A flexible framework for numerical simulations with spectral methods. Phys. Rev. Res. 2020, 2, 023068.

Busse, F.H. and Schubert, G., Convection in a fluid with two phases. J. Fluid. Mech. 1971, 46, 801–812. Byrne, M.P. and O'Gorman, P.A., The response of precipitation minus evapotranspiration to climate warming: why the "wet-get-wetter, dry-get-drier" scaling does not hold over land. J. Clim. 2015, **28**, 8078–8092.

Chandrasekhar, S., Hydrodynamic and Hydromagnetic Stability, 1961 (New York: Oxford University Press).



- Cheng, K.Y., Harris, L., Bretherton, C., Merlis, T.M., Bolot, M., Zhou, L., Kaltenbaugh, A., Clark, S. and Fueglistaler, S., Impact of warmer sea surface temperature on the global pattern of intense convection: insights from a global storm resolving model. Geophys. Res. Lett. 2022, 49, e2022GL099796.
- Christopher, T., Le Bars, M. and Llewellyn Smith, S.G., Linear and nonlinear stability of Rayleigh-Bénard convection with zero-mean modulated heat flux. J. Fluid Mech. 2023, 961, A1-1-A1-25.
- Guichard, F. and Couvreux, F., A short review of numerical cloud-resolving models. Tellus A: Dyn. Meteorol. Oceanogr. 2017, 69, 1373578.
- Hartmann, D.L., Dygert, B.D., Blossey, P.N., Fu, Q. and Sokol, A.B., The vertical profile of radiative cooling and lapse rate in a warming climate. J. Clim. 2022, 35, 6253-6265.
- Held, I.M. and Soden, B.J., Robust responses of the hydrological cycle to global warming. J. Clim. **2006**, **19**, 5686–5699.
- Jeevanjee, N. and Fueglistaler, S., Simple spectral models for atmospheric radiative cooling. J. Atmos. Sci. 2020, 77, 479-497.
- Kendon, E.J., Stratton, R.A., Tucker, S., Marsham, J.H., Berthou, S., Rowell, D.P. and Senior, C.A., Enhanced future changes in wet and dry extremes over Africa at convection-permitting scale. Nat. Commun. 2019, 10, 1-14.
- Malkus, W.V., The amplitude of convection. Evolut. Phys. Oceanogr. 1981, 384-393.
- Marston, J. and Tobias, S., Recent developments in theories of inhomogeneous and anisotropic turbulence. Annu. Rev. Fluid Mech. 2023, 55, 351-375.
- Muller, C. and Takayabu, Y., Response of precipitation extremes to warming: what have we learned from theory and idealized cloud-resolving simulations, and what remains to be learned? Environ. Res. Lett. 2020, 15, 035001.
- Muller, C.J., O'Gorman, P.A. and Back, L.E., Intensification of precipitation extremes with warming in a cloud-resolving model. J. Clim. 2011, 24, 2784-2800.
- O'Gorman, P.A., Precipitation extremes under climate change, Curr. Clim. Change Rep. 2015, 1,
- Oishi, J.S. and Brown, B.P., On the linear stability of partially and fully saturated atmospheres to moist convection, 2024.
- Pauluis, O. and Schumacher, J., Idealized moist Rayleigh-Bénard convection with piecewise linear equation of state. Commun. Math. Sci. 2010, 8, 295-319.
- Phillips, N.A., The equations of motion for a shallow rotating atmosphere and the "traditional approximation". J. Atmos. Sci. 1966, 23, 626-628.
- Randall, D.A. and Wang, J., The moist available energy of a conditionally unstable atmosphere. J. Atmos. Sci. 1992, 49, 240-255.
- Robe, F.R. and Emanuel, K.A., Moist convective scaling: some inferences from three-dimensional cloud ensemble simulations. J. Atmos. Sci. 1996, 53, 3265–3275.
- Roland Stull, 4.0: Vapor pressure at saturation, 2024. Available online at: https://geo.libretexts.org/ Bookshelves/Meteorology and Climate Science/Practical Meteorology (Stull)/04%3A Wate r_Vapor/4.00%3A_Vapor_Pressure_at_Saturation (accessed 18 December 2024).
- Schär, C., Fuhrer, O., Arteaga, A., Ban, N., Charpilloz, C., Girolamo, S.D., Hentgen, L., Hoefler, T., Lapillonne, X., Leutwyler, D., Osterried, K., Panosetti, D., Rüdisühli, S., Schlemmer, L., Schulthess, T.C., Sprenger, M., Ubbiali, S. and Wernli, H., Kilometer-scale climate models: prospects and challenges. Bull. Am. Meteorol. Soc. 2020, 101, 567-587.
- Seager, R., Naik, N. and Vecchi, G.A., Thermodynamic and dynamic mechanisms for large-scale changes in the hydrological cycle in response to global warming. J. Clim. 2010, 23, 4651-4668.
- Singh, M.S. and O'Gorman, P.A., Influence of entrainment on the thermal stratification in simulations of radiative-convective equilibrium. Geophys. Res. Lett. 2013, 40, 4398-4403.
- Tailleux, R. and Grandpeix, J.Y., On the seemingly incompatible parcel and globally integrated views of the energetics of triggered atmospheric deep convection over land. Quart. J. R. Meteorol. Soc. 2004, 130, 3223-3243.
- Tomassini, L. and Yang, G.Y., Tropical moist convection as an important driver of Atlantic Hadley circulation variability. Quart. J. R. Meteorol. Soc. 2022, 148, 3287-3302.



Tomassini, L., Willett, M., Sellar, A., Lock, A., Walters, D., Whitall, M., Sanchez, C., Heming, J., Earnshaw, P., Rodriguez, J.M., Ackerley, D., Xavier, P., Franklin, C. and Senior, C.A., Confronting the convective gray zone in the global configuration of the met office unified model. I. Adv. Model. Earth Syst. 2023, 15, e2022MS003418.

Vallis, G.K., Water vapour and the tropical atmosphere. In Atmospheric and Oceanic Fluid Dynamics: Fundamentals and Large-Scale Circulation, pp. 673-728, 2017 (Cambridge University Press: Cambridge).

Vallis, G.K., Parker, D.J. and Tobias, S.M., A simple system for moist convection: the Rainy-Bénard model. J. Fluid Mech. 2019, 862, 162-199.

Waleffe, F., Boonkasame, A. and Smith, L.M., Heat transport by coherent Rayleigh-Bénard convection. Phys. Fluids 2015, 27, 051702-1-051702-7.

Wing, A.A., Reed, K.A., Satoh, M., Stevens, B., Bony, S. and Ohno, T., Radiative-convective equilibrium model intercomparison project. Geosci. Model Dev. 2018, 11, 793-813.

Yano, J.I., Chapter 3 - Rayleigh-Bénard convection. In Geophysical Convection Dynamics, Developments in Weather and Climate Science, edited by J.I. Yano, Vol. 5 of Developments in Weather and Climate Science, pp. 29-47, 2023 (Elsevier: Amsterdam, Netherlands).

Yano, J.I., Chaboureau, J.P. and Guichard, F., A generalization of CAPE into potential-energy convertibility. Quart. J. R. Meteorol. Soc. 2005, 131, 861–875.

Appendices

Appendix A. implicit global warming

Instead of imposing a surface temperature increase in the perturbation temperature, with a constant reference state of $\theta_0 = T_0 = 300$ K, we present here an implicit method for a small variation in the surface temperature by modifying the reference temperature directly.

Let $T_0 = \overline{T_0} + \Delta T_0$, with $\overline{T_0} \equiv 300 \text{ K}$ and \overline{f} representing parameter f's value for $T_0 = \overline{T_0}$, we can fully examine the effect of increasing the surface temperature on this system. Starting with the Clausius-Clapyeron relationship,

$$e_s = \overline{e_0} \exp\left\{\frac{L}{R_v} \left(\frac{1}{\overline{T_0}} - \frac{1}{T}\right)\right\},$$
 (A.1)

Substituting $T = T_0 + \delta T$ and assuming $\overline{T_0} \gg \delta T + \Delta T_0$, we can approximate (A.1) by:

$$e_s pprox \overline{e_0} \exp \left\{ rac{L}{R_{
u}} \left(rac{\Delta T_0 + \delta T}{\overline{T_0}^2}
ight)
ight\}.$$

Which after some manipulation can be written (using a first order Taylor expansion) as,

$$e_s \approx \overline{e_0} \left(1 + \frac{L}{R_v \overline{T_0}^2} \Delta T_0 \right) \exp \left\{ \frac{L}{R_v \overline{T_0}^2} \delta T \right\}.$$

It follows that,

$$e_0(\Delta T_0) \approx \overline{e_0} \left(1 + \frac{L}{R_\nu \overline{T_0}^2} \Delta T_0 \right).$$
 (A.2)

As before, we express the pressure as,

$$p \approx p_0 \exp \left(\frac{c_p}{R_d T_0} \delta T \right) \approx p_0 \exp \left\{ \frac{c_p}{R_d \overline{T_0}} \left(1 - \frac{\Delta T_0}{2 \overline{T_0}} \right) \delta T \right\},$$

So that the saturation specific humidity can be approximated,

$$q_s = \epsilon \frac{e_s}{p} \approx \epsilon \frac{\overline{e_0}}{p_0} \left(1 + \frac{L}{R_{\nu} \overline{T_0}^2} \Delta T_0 \right) \exp \left\{ \frac{L}{R_{\nu} \overline{T_0}^2} \delta T - \frac{c_p}{R_d \overline{T_0}} \left(1 - \frac{\Delta T_0}{\overline{T_0}} \right) \delta T \right\},$$

$$\Rightarrow q_s \approx q_0(\Delta T_0) \exp\left(\alpha(\Delta T_0)\delta T\right),\tag{A.3}$$

where,

$$q_0(\Delta T_0) \approx \overline{q_0} + \frac{L\overline{q_0}}{R_\nu \overline{T_0}^2} \Delta T_0,$$
 (A.4)

and,

$$\alpha(\Delta T_0) \approx \overline{\alpha} + \frac{c_p}{R_d T_0^2} \Delta T_0.$$
 (A.5)

We also have the gamma parameter, $\gamma = gL/(c_p\theta_0)$, and since $\theta_0 = \overline{T_0} + \Delta T_0$, we can write

$$\gamma \left(\Delta T_0 \right) = \overline{\gamma} - \frac{\overline{\gamma}}{2\overline{T_0}} \Delta T_0 \tag{A.6}$$

We are interested in the non-dimensional parameters, under the same dry adiabatic non-dimensionalisation as in section 2.2. Recall that $[T] = gH/c_p$ is independent of the reference temperature T_0 , but $[B] = g^2H/(c_p\theta_0) \approx \overline{[B]} - \frac{\overline{[B]}}{2T_0}\Delta T_0$, i.e. the buoyancy scale decreases with increasing surface temperature. We note that the non-dimensional parameters which depend on θ_0 or/and ΔT_0 are:

$$Ra = \frac{g^2 H^4}{\theta_0 c_p \nu \kappa}, \quad \hat{\gamma} = \frac{q_0 (\Delta T_0) L}{g H}, \quad \hat{\tau} = \frac{\tau g}{(c_p \theta_0)^{1/2}}, \quad \hat{r} = \frac{(c_p^3 \theta_0)^{1/2} r}{g^2 H}, \quad \hat{\alpha} = \frac{g H \alpha (\Delta T_0)}{c_p} \quad (A.7)$$

We then want to write the parameters in terms of the non-dimensionalised surface temperature increase, $\Delta \hat{T}_0 = \Delta T_0/[T]$. Note that $\overline{T}_0 \approx 3[T]$. Expanding about θ_0 about T_0 , we can write the non-dimensional parameters as:

$$Ra(\Delta \hat{T}_0) \approx \overline{Ra} \left(1 - \frac{1}{3} \Delta \hat{T}_0 \right),$$
 (A.8)

$$\gamma \left(\Delta \hat{T}_{0}\right) \approx \overline{\gamma} \left(1 + \frac{L}{3R_{v}\overline{T_{0}}} \Delta \hat{T}_{0}\right) \approx \overline{\gamma} \left(1 + 6\Delta \hat{T}_{0}\right),$$
 (A.9)

$$\tau(\Delta \hat{T}_0) \approx \overline{\tau} \left(1 - \frac{1}{6} \Delta \hat{T}_0 \right),$$
(A.10)

$$r(\Delta \hat{T}_0) \approx \bar{r} \left(1 + \frac{1}{6} \Delta \hat{T}_0 \right),$$
 (A.11)

and,

$$\alpha(\Delta \hat{T}_0) \approx \overline{\alpha} + \frac{gH}{3R_d T_0} \Delta \hat{T}_0 \approx \overline{\alpha} + 3.8 \Delta \hat{T}_0$$
 (A.12)

Note that we only consider surface temperature increases up to $\sim 10K$, i.e $\Delta \hat{T}_0 \leq 0.1$. The dominant parameter changing is γ , due to the nature of the Clausius-Clapyeron relation. Changes in Ra, $r \& \tau$ are almost negligible, due to the range of surface temperature increases we consider in our analysis. Also notice that by using the leading order approximation $(p=p_0)$ presented in Vallis $et\ al.\ (2019)$, the dependence of the surface temperature in α above can be removed.

In figure A1, we show a comparison of the temperature profiles of the solution where the surface temperature is changed explicitly (as in the main body), and implicitly (by changing the parameters above) for surface temperatures of 305 K (blue) and 310 K (red). There is a slight difference in the upper part of the profiles, but the profiles show a similar qualitative change with surface temperature for both methods. While the implicit method of varying the non-dimensional may be more consistent, it does not allow for easy understanding and implementation of a climate change scenario. The scales of the parameters are changing as a function of the surface temperature, which does not allow straightforward comparison of the solutions.

The analysis above provides a mapping between the explicit and implicit methods for imposing a surface temperature increase. The implicit approach to global warming is more consistent

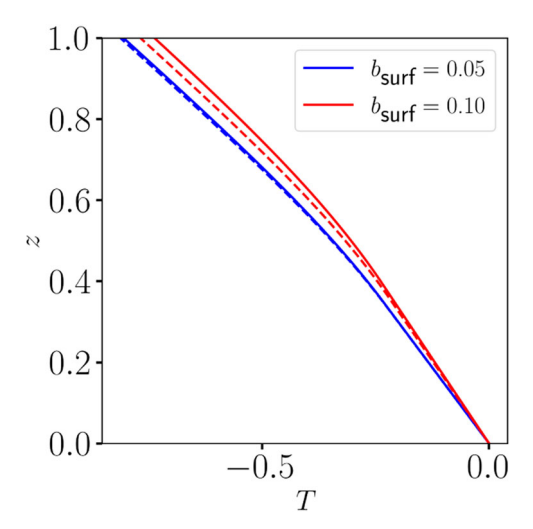


Figure A1. Comparison of the temperature profiles for the explicit (solid) and implicit (dashed) methods of imposing a surface temperature in crease. For the explicit case, we plot $\delta T - b_{\text{surf}}$ to allow direct comparison with the implicit solution, which has $\delta T(0) = 0$. The base parameter values are $\overline{Ra} = 10^6$, $RH_{\text{surf}} = 0.6$, $\overline{\tau} = 0.05$, $\overline{\alpha} = 6.0$, & $\overline{\gamma} = 0.25$ (Colour online).

with the model assumptions than the explicit approach. However, the modification of the reference temperature and potential temperature (T_0, θ_0) causes the scales used in the dry adiabatic non-dimensionalisation to change, which makes the comparison of the different climate change scenarios more difficult to interpret. Due to the range of surface temperatures considered in our analysis, the explicit and implicit methods provide only slightly different results. We note that while less consistent than the implicit method, the explicit method captures the key effects of a surface temperature increase: warmer domain temperatures, a Clausius-Clapyeron scale increase in the moisture, and increased curvature of the moist adiabat.

Appendix B. CAPE for the dry system

From Wallefe and Smith 2015, the classic Rayleigh-Bénard convection equations are:

$$\frac{D\mathbf{u}}{Dt} = -\nabla \phi + g\alpha_{\nu} T\mathbf{k} + \nu \nabla^{2} \mathbf{u}, \tag{B.1}$$

$$\frac{DT}{Dt} = \kappa \nabla^2 T. \tag{B.2}$$

Note that temperature here is equivalent to buoyancy in our model. A surface parcel would maintain its temperature on adiabatic ascent (DT/Dt = 0), and so the parcel profile is given by $T_p(z) = T_0$. The basic state solution, for fixed temperature boundary conditions $T(0) = T_0$, $T(H) = T_1$ is,

$$T = T_0 - \frac{\Delta T}{H} z,\tag{B.3}$$

where $\Delta T \equiv T_0 - T_1$. As in section 2.4, we take the environment to be the basic state, and we calculate the (dry) CAPE as:

CAPE =
$$\int_{0}^{H} (T_p - T_E) dz = \frac{\Delta T}{H} \int_{0}^{H} z dz = \frac{H \Delta T}{2}$$
 (B.4)

Note that $T_D \ge T_E$ at all heights, so pCAPE = CAPE, CIN = 0, LFC = 0, and LNB = H. Recalling the expression for the Rainy number (equation (26)), it follows that,

$$Ry = \frac{H^3 \Delta T}{2\kappa \nu} = \frac{Ra}{2g\alpha_{\nu}}.$$
 (B.5)

Therefore, the Rainy number is directly proportional to the classical Rayleigh number for the dry system.

Appendix C. radiative rainy number

We rescale the dry adiabatic non-dimensionalisation, using the minimum moist static energy gradient of the basic state to set the timescale, and the height of the domain to set the length scale. Note that, from equation (31),

$$\frac{\mathrm{d}m}{\mathrm{d}z} = rRa^{1/2}(z-1). \tag{C.1}$$

Next, we recall the alternative definition of conditional instability is dm/dz < 0 and db/dz > 0, and note that dm/dz is a minimum at z = 0. Writing,

$$-\min\left(\frac{\mathrm{d}m}{\mathrm{d}z}\right) \sim \frac{[B]}{[L]} = \frac{1}{[t]^2},$$

and taking [L] = 1 (non-dimensional height of the domain), the new scales can be written as:

$$[t] = \frac{1}{r^{1/2} Ra^{1/4}}, \quad [L] = 1, \quad [B] = r Ra^{1/2}, \quad [U] = \frac{[L]}{[t]} = r^{1/2} Ra^{1/4}.$$
 (C.2)

Note that the (instability) timescale decreases with r and Ra, and the velocity and buoyancy scales increase with r and Ra. After some algebra, the rescaled momentum equation can be written as:

$$\frac{D\hat{\mathbf{u}}}{D\hat{t}} = --\nabla\hat{\phi} + \hat{b}\mathbf{k} + \frac{1}{R\gamma_p^{3/4}}\nabla^2\hat{\mathbf{u}},\tag{C.3}$$

where the Radiative Rainy number is defined as,

$$Ry_R \equiv r^{2/3} Ra. \tag{C.4}$$

Note that Ra_R/Ry at criticality shows a variation of $\sim 20\%$. This (approximate) proportionality reveals the relationship,

pCAPE
$$\sim \frac{r^{2/3}}{(1 - \text{LFC})^2}$$
, (C.5)

at least for constant surface relative humidity ($RH_{surf} = 0.6$). The relationship for the different climate chance scenarios is shown in figure C2. The ratio does not vary significantly with radiation, relative to the changes with surface humidity or surface temperature.

Appendix D. parameter correction

In Vallis *et al.* (2019), the value of the constant $e_0 = 611$ Pa in equation (2.16) is valid for a reference temperature of $T_0 = 273$ K (Roland Stull 2024), rather than the specified reference temperature of $T_0 = 300 \text{ K}$ used throughout the rest of the paper. Letting $\theta_0 = 300 \text{ K}$, $T_0 = 273 \text{ K}$, and expressing $T = \theta_0 + \delta T$, we can write the saturation vapor pressure equation (2.16) as,

$$e_s = e_0 \exp\left(\frac{L}{R_v} \left\{ \frac{1}{T_0} - \frac{1}{\theta_0 + \delta T} \right\} \right). \tag{D.1}$$

Assuming $\theta_0 \gg \delta T$, equation (D.1) can be approximately written as

$$e_s \approx e_0 \exp\left(\frac{L}{R_{\nu}} \left\{ \frac{\theta_0 - T_0}{T_0 \theta_0} \right\} \right) \exp\left(\frac{L}{R_{\nu}} \left\{ \frac{\delta T}{T_0 \theta_0} \right\} \right).$$
 (D.2)

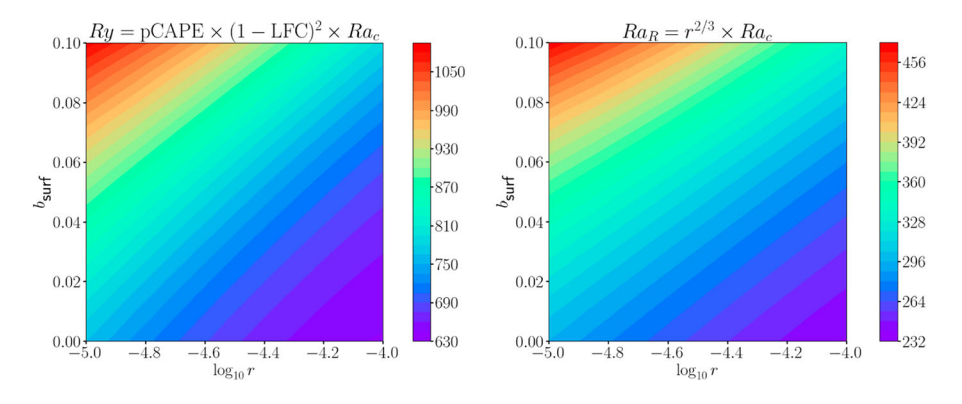


Figure C1. Critical Rainy number (left) and critical Radiative Rainy number (right). Both Rainy numbers are based on different quantifications of conditional instability, and show a degree of proportionality. (Colour online).

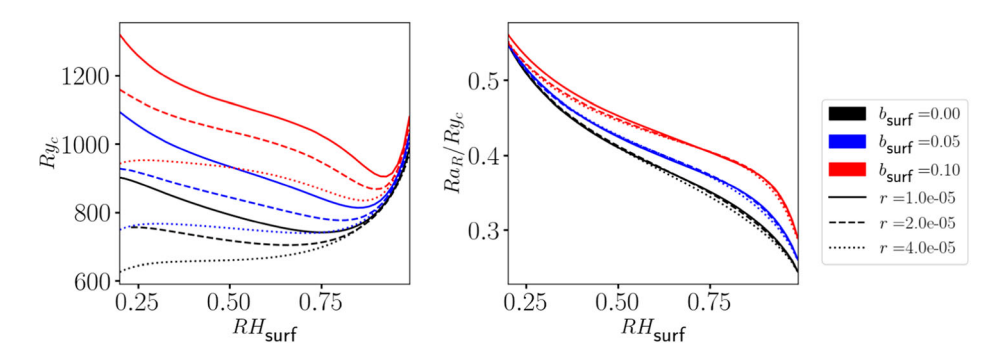


Figure C2. Ratio of the critical Rainy number to the critical Radiative Rainy number. (Colour online).

Recall the approximate relationship between the saturation vapor pressure and saturation specific humidity given by equation (2.18),

$$q_s pprox \epsilon \frac{e_s}{p}$$
. (D.3)

Using equation (2.21), the pressure can be approximately written by,

$$p \approx p_0 \exp\left(\frac{c_p \delta T}{R_d \theta_0}\right).$$
 (D.4)

Combining equations (D.2)–(D.4), the saturation vapor pressure can be expressed as,

$$q_s = \epsilon \frac{e_0}{p_0} \exp\left(\frac{L}{R_v} \left\{ \frac{\theta_0 - T_0}{T_0 \theta_0} \right\} \right) \exp\left(\left\{ \frac{L}{R_v \theta_0 T_0} - \frac{c_p}{R_d \theta_0} \right\} \delta T \right),$$

or,

$$q_s = q_0 \exp{(\alpha \delta T)},\tag{D.5}$$

where,

$$q_0 = \epsilon \frac{e_0}{p_0} \exp\left(\frac{L}{R_v} \left\{ \frac{\theta_0 - T_0}{T_0 \theta_0} \right\} \right) = 0.019 \,\mathrm{kg \, kg^{-1}},$$
 (D.6)

and,

$$\alpha = \frac{L}{R_{\nu}\theta_0 T_0} - \frac{c_p}{R_d \theta_0} = 0.054 \,\mathrm{K}^{-1}.\tag{D.7}$$



Note that in Vallis *et al.* (2019), $\alpha = 0.060 \, \mathrm{K}^{-1}$, and $q_0 = 3.8 \times 10^{-3} \, \mathrm{kg \, kg^{-1}}$, which is five times smaller than the value found in equation (D.6). The discrepancy in these parameters affects the values of the non-dimensional parameters α and γ in the Rainy-Bénard model.